Journal of Controlled Release 373 (2024) 277–292

Contents lists available at ScienceDirect

Journal of Controlled Release

journal homepage: www.elsevier.com/locate/jconrel

Nanotechnology-assisted intracellular delivery of antibody as a precision therapy approach for KRAS-driven tumors

Ana M. López-Estévez [a,b,c], Lucía Sanjurjo [a,b], Ángela Turrero [a], Iker Arriaga [d], Nicola G. A. Abrescia [d,e], Ana Poveda [f], Jesús Jiménez-Barbero [e,f], Anxo Vidal [a], Dolores Torres [c], María José Alonso [a,b,c,*]

[a] Center for Research in Molecular Medicine and Chronic Diseases (CiMUS), University of Santiago de Compostela, 15782 Santiago de Compostela, Spain
[b] Health Research Institute of Santiago de Compostela, 15782 Santiago de Compostela, Spain
[c] Department of Pharmacology, Pharmacy and Pharmaceutical Technology, School of Pharmacy, University of Santiago de Compostela, 15782 Santiago de Compostela, Spain
[d] Structure and Cell Biology of Viruses Lab, CIC bioGUNE, Basque Research and Technology Alliance (BRTA), 48160 Derio, Spain
[e] Ikerbasque, Basque Foundation for Science, 48009 Bilbao, Spain
[f] Chemical Glycobiology Laboratory, CIC bioGUNE, Basque Research and Technology Alliance (BRTA), 48160 Derio, Spain

ARTICLE INFO

Keywords:
KRAS
cancer
Intracellular
mAb/monoclonal antibody
Targeted delivery
Nanotechnology

ABSTRACT

The Kirsten Rat Sarcoma Virus (KRAS) oncoprotein, one of the most prevalent mutations in cancer, has been deemed undruggable for decades. The hypothesis of this work was that delivering anti-KRAS monoclonal antibody (mAb) at the intracellular level could effectively target the KRAS oncoprotein. To reach this goal, we designed and developed tLyP1-targeted palmitoyl hyaluronate (HAC16)-based nanoassemblies (HANAs) adapted for the association of bevacizumab as a model mAb. Selected candidates with adequate physicochemical properties (below 150 nm, neutral surface charge), and high drug loading capacity (>10%, *w*/w) were adapted to entrap the antiKRAS^{G12V} mAb. The resulting antiKRAS^{G12V}-loaded HANAs exhibited a bilayer composed of HAC16 polymer and phosphatidylcholine (PC) enclosing a hydrophilic core, as evidenced by cryogenic-transmission electron microscopy (cryo-TEM) and X-ray photoelectron spectroscopy (XPS). Selected prototypes were found to efficiently engage the target KRAS^{G12V} and, inhibit proliferation and colony formation in KRAS^{G12V}-mutated lung cancer cell lines. *In vivo*, a selected formulation exhibited a tumor growth reduction in a pancreatic tumor-bearing mouse model. In brief, this study offers evidence of the potential to use nanotechnology for developing anti-KRAS precision therapy and provides a rational framework for advancing mAb intracellular delivery against intracellular targets.

1. Introduction

Despite the great advances in cancer therapy and the emergence of personalized medicine, the majority of intracellular oncoproteins remain undrugged. A particularly relevant example of the so-called *undruggable* targets is the RAS family, whose mutated forms are present in 9–30% of human cancers [1,2]. Mutations in RAS are responsible for the accumulation of RAS proteins in the GTP-bound state leading to a permanent “on” conformation of the protein, triggering the activation of RAS-dependent downstream signaling pathways, which ultimately promote cellular proliferation and angiogenesis while interfering with apoptosis [3–5].

Being the most frequently mutated oncogene, Kirsten Rat Sarcoma Virus (KRAS) has attracted substantial attention. In the clinical setting, KRAS^{G12V} T-cell-based therapies have found their way into phase I-II clinical trials (NCT04146298, NCT03190941), although scarce information is known about their general outcome. Recently, a lymph-node-targeting amphiphilic platform incorporating vaccine peptides against KRAS G12D and G12R has shown to induce T cell response (Phase I, NCT04853017) [6]. Despite this recent success, the necessity of specifically inhibiting KRAS mutations for successful therapy has been argued [7]. Unfortunately, the two small molecules inhibitors, sotorasib and

---

* Corresponding author at: Center for Research in Molecular Medicine and Chronic Diseases (CiMUS), University of Santiago de Compostela, 15782 Santiago de Compostela, Spain.

E-mail address: mariaj.alonso@usc.es (M.J. Alonso).

https://doi.org/10.1016/j.jconrel.2024.07.032
Received 14 May 2024; Received in revised form 3 July 2024; Accepted 12 July 2024

adagrasib [8,9], recently marketed for specifically target KRAS^{G12C}, have not been as efficacious as expected in the clinical setting [10]. This has prompted the exploration of alternative strategies at the preclinical level, with a focus on targeting the KRAS signaling pathway. Among these strategies is targeting RAS with ankyrin repeat proteins [11]' with small interfering RNA (siRNA) standing out [12–16]· While this approach has led to promising data, it remains at an early stage of evidence.

Based on the limited success of the so far explored strategies, our hypothesis has been that the use of monoclonal antibodies (mAbs) with large surface area paratopes capable of facilitating protein-protein interactions (PPIs) has the potential to be a therapeutic option. To overcome the inherent limitations of mAbs for diffusing across biological barriers some researchers have engineered mAb with covalent modifications, incorporating cytosol-penetrating motifs. Although the results obtained in murine models of carcinomas look somehow promising [17,18], there are still pending issues such as the targeting to the tumor and the potential immunotoxicity associated to its off-target accumulation.

In our lab, we have gone a step forward and chosen nanotechnology as an enabling technology for helping mAbs overcoming biological obstacles and facilitating their access to intracellular targets [19–22]. More precisely, we have developed a platform particularly adapted for the intracellular delivery of mAbs [21]. By engineering HA-based nanocapsules, we successfully delivered an anti-gasdermin B mAb, addressing the intracellular oncoprotein gasdermin B. This led to a reduced tumor growth and diminished lung metastasis in an orthotopic mammary fat pad tumor-bearing mouse model. The nanotechnology approach has been also explored for targeting other oncoproteins as is the case of transferrin targeted- poly-lactic-*co*-glycolic acid nanoparticles (NPs) for delivering antiBCR/ABL mAb [20] or antiMYC mAb-loaded polymeric micelles [19]. The knowledge generated from these approaches have facilitated the development of the earliest antiKRAS mAb-Pluronic™ F127 -based micelles. Although some preliminary promising data in KRAS^{G13D}-mutant tumors have been achieved [22], the poor loading capacity and the uncontrolled biodistribution have remained challenging. Despite the efforts invested in these approaches, none have specifically target the KRAS^{G12V} mutation, which exhibits one of the highest incidences in solid tumors such as pancreatic cancer [23,24].

As a disruptive alternative to the aforementioned technologies and recognizing the absence of available treatments for the KRAS^{G12V} mutation, this study validates the palmitoyl hyaluronate (HAC16)-based nanoassemblies (HANAs) technology [25] for the intracellular delivery of the antiKRAS^{G12V} mAb. To ensure the NPs accumulation in the tumor tissue, our lab and others have identified the truncated LyP-1 (tLyP1) peptide as an excellent candidate to enhance the NPs uptake and intratumoral diffusion [26–28]. Indeed, we have demonstrated that the surface functionalization of docetaxel-loaded nanocapsules with tLyP1 leads to a 36.6-fold increase in tumor accumulation over the free cytotoxic agent [26]· Building on this foundation, we have engineered a synthetic approach for the obtention of tLyP1-conjugates and further use them for the development of tLyP1-targeted HANAs entrapping a model mAb, bevacizumab (BVZ). Afterwards, we adapted the HANAs technology for the association of the antiKRAS^{G12V} mAb. Furthermore, we assayed the efficacy and capacity to directly target the KRAS^{G12V} oncoprotein after antiKRAS^{G12V} mAb internalization in KRAS^{G12V} mutant lung cancer cell lines. Finally, the antitumoral efficacy was evaluated *in vivo* using a KRAS^{G12V} mutant subcutaneous pancreatic murine model.

2. Materials and methods

2.1. Materials

The humanized mAb bevacizumab was kindly donated by mAbxience (Spain). AntiKRAS^{G12V} mAb **was acquired from** bioGenes GmbH (Germany). Sodium palmitoyl hyaluronate MW 30-70 kDa DS 1–10% and DS 10–15% were obtained from Contipro a.s. (Czech Republic). Phosphatidylcholine from Soybean (Lipoid S100) was provided by Lipoid GmbH (Germany). 1,2-distearoyl-sn-glycero-3-phosphoethanolamine-N-[methoxy (polyethylene glycol)2000 - maleimide] (DSPE. PEG$_{2000}$-Mal) was acquired from Avanti Polar lipids (Alabaster, USA). The truncated LyP-1 peptide (aminoacidic sequence: CGNKRTR) was synthesized by ChinaPeptides Co., Ltd. (Shanghai, China). Fetal bovine serum (FBS) was provided by Gibco (Thermo Fisher Scientific, United States). Methanol-D4 (CD_3OD), deuteration degree 99.8%, and antiKRAS mAb produced in mice acquired from clone 3B10—2F2 were provided by Merck (Darmstadt, Germany). Resazurin sodium salt, Triton X-100, Accutase®, 2-(N-Morpholino)ethanesulfonic acid hydrate (MES) buffer, N-hydroxysuccinimide (NHS) and N-Ethyl-N′-(3-dimethylaminopropyl)carbodiimide (EDC), N-(2-Aminoethyl)maleimide trifluoroacetate salt (Mal), HEPES buffer, deuterium oxide (D_2O), dimethyl sulfoxide-d_6 (DMSO-d_6), TBS lysis buffer [20 mM Tris, pH 7.5, containing 150 mM NaCl, 1 mM EDTA, 1 mM EGTA, 1% Triton X-100, 1 mM Na3VO4, 1 mM PMSF, and complete protease inhibitor cocktail] were obtained from Sigma-Aldrich (Darmstadt, Germany). Triethylamine (TEA) was purchased from Scharlab (Barcelona, Spain). Tris(2-carboxyethyl)phosphine hydrochloride (TCEP) was purchased from Alfa Aesar (Kandel, Germany). Polyvinylidene difluoride (PVDF) protein blotting membrane were acquired from SERVA Electrophoresis GmbH (Heidelberg, Germany). The 96 multiwells plate, SnakeSkin™ Dialysis Tubing (regenerated cellulose, SnakeSkin 7 K MWCO, 22 mm), anti-mouse IgG DyLight™ 680 Ab and anti-rabbit IgG DyLight™ 800 Ab produced in goat, pierce Ip lysis buffer, RPMI 1640, Dulbecco's Modified Eagle Medium (DMEM), F(ab')2-Goat anti-Mouse IgG (H + L) secondary antibody PE, and BCA protein assay reagent kit were provided by Thermo Fisher Scientific (United States). Goat anti-human IgG HRP conjugated was obtained from Jackson Immuno Research Laboratories, Inc. (United States). 2,2′-azino-di-(3-ethylbenzthiazoline sulfonic acid (ABTS) solution was acquired from Roche (Switzerland). SYPRO® Ruby was purchased from Lonza (Basel, Switzerland). Protein G PLUS-agarose beads and mAb anti-alpha tubulin were acquired from Santa Cruz Biotechnologies (United States). MAbs anti-phosphorylated-p44/42 MAPK (Erk1/2) (Thr202/Tyr204) (9106), and anti-p44/42 MAPK (Erk1/2) (137F5), were purchased from Cell Signaling Technology.

2.2. Synthesis of tLyP1-targeted conjugates

2.2.1. Palmitoyl hyaluronate (HAC16)-tLyP1

The functionalization of the HAC16 MW 30-70 kDa DS 1–10% with the tLyP1 peptide was carried out in two-steps reaction. Prior to it, stocks solutions were dissolved as follows: HAC16 (4 mg/mL) in 40% (*v*/v) EtOH in ultrapure water, EDC (20.8 mg/mL), and Mal (267 mg/mL) in ultrapure water whereas NHS (20.8 mg/mL) in EtOH. Over the HAC16 (5 mL), it was subsequently added 100 μL MES buffer pH 6 (adjusted with TEA), 71.9 μL EDC for 5 min at RT, 86.4 μL NHS for 10 min at room temperature (RT), and 7.4 μL Mal for 2 h at 40 °C under magnetic stirring. The product was purified by dialysis against EtOH: NaCl 150 mM (50%, v/v EtOH/ultrapure water). The resulting HAC16-Mal conjugate was frozen at −80 °C and freeze-dried (Genesis™ 25 EL, S·P Industries, PA, USA). Thereafter, the tLyP1 peptide was anchored to the HAC16-Mal intermediate by mixing the polymer (4 mg/mL) with the peptide in the presence of TCEP under magnetic stirring at RT. The reaction was carried out in HEPES buffer 10 mM (60% (*v*/v) EtOH in ultrapure water, pH 7.2) at a roughly determined tLyP1:Mal molar ratio of 1:1. The resulting conjugate was purified by dialysis against EtOH:NaCl 150 mM (60%, v/v) and ultrapure water. Afterward, the HAC16-tLyP1 conjugate was frozen at −80 °C, freeze-dried, and stored at −20 °C.

HAC16 MW 30-70 kDa DS 10–15% synthesis was carried out in a molar ratio HAC16:EDC:NH:Mal (1,0.164:0.328:0.324) following above-described methods modified accordingly. Therefore, the polymer was dissolved in a volume ratio EtOH:ultrapure water of 1:1, keeping these conditions during the reaction procedure. For the tLyP-1 incorporation, the HAC16-mal intermediate was dissolved in HEPES buffer 10 mM at pH 7.2 (prepared in EtOH:ultrapure water in a volume ratio of 1:1.5 adjusted with NaOH 10 M) at an initial concentration of 4 mg/mL; tLyP1 and TCEP were dissolved in the same buffer at initial concentrations of 0.65 and 0.22 mg/mL. The reaction was kept overnight under magnetic agitation at 300 rpm. Then, the conjugate was purified as previously described but against EtOH:NaCl 150 mM (volume ratio, 1:1). The purified conjugate was freeze-dried and stored.

2.2.2. DSPE.PEG$_{2K}$-tLyP1

Stock solutions of DSPE-PEG$_{2K}$-Mal (40 mg/mL) and tLyP1 (1 mg/mL) in HEPES buffer 10 mM (60% (*v*/v) EtOH in ultrapure water, pH 7.2) were prepared. The peptide was added to the DSPE.PEG$_{2K}$-Mal at a molar ratio of 2:1 tLyP1: DSPE.PEG$_{2K}$-Mal and let it stir at RT overnight. Afterward, the free tLyP1 was removed by dialyzing against 150 mM NaCl (2 h) and then, two more cycles against ultrapure water. Finally, the functionalized lipid was freeze-dried, and stored at −20 °C.

2.2.3. ^{1}H NMR spectroscopy

^{1}H NMR spectra were recorded using a Bruker DRX-500 or NEO-750 spectrometer. HAC16-Mal intermediate, HAC16-tLyP1, and DSPE.PEG$_{2K}$-tLyP1 were dissolved in CD_3OD/D_2O, phosphate buffer saline D_2O/CD_3OD (1/1, *v*/v) at pH 7.4 and DMSO-d_6 at 2 mg/mL, respectively. When required, trimethylsilylpropanoic acid was used as an internal reference. ^{1}H NMR spectra were recorded at 300 K, 64 to 2048 accumulated scans and a relaxation delay of 8–12 s Spectral analysis was done by using the MestreNova Software (Mestrelab Research S.L.), and the extent of the conjugation was calculated as the number of double bond of the maleimide or tLyP1 molecules per 100 carboxylic acid groups of HAC16 or methyl groups from the DSPE.PEG$_{2K}$.

2.3. Preparation of BVZ-loaded non-targeted HANAs

HANAs were prepared following an assembling technique previously described by our lab. [25] Briefly, to 500 μL of an 40% *v*/v ethanol/ultrapure water HAC16 30-70 kDa DS 1–10% solution (4 mg/mL, stock concentration) were added 125 μL of an aqueous solution of BVZ (16 mg/mL, stock concentration) under magnetic stirring at 1100 rpm and RT. Subsequently, 50 μL of an ethanolic solution of Lipoid S100 (20 mg/mL, stock concentration) were added dropwise over the above mixture. Finally, the volume was made up to 1 mL with PBS.

In the case of HANAs containing the PEGylated lipid (**PEG-NAs**), the above method was modified accordingly. To 500 μL of HAC16 at 0.5 mg/mL were added 125 μL of BVZ (4 mg/mL, stock concentration) under magnetic stirring at 1100 rpm and RT. Subsequently, 50 μL of an ethanolic solution containing equal volumes of Lipoid S100 at 20 mg/mL and DSPE.PEG$_{2K}$ at 0.04 mg/mL were added dropwise over the above mixture. Finally, the volume was made up to 1 mL with PBS.

HANAs were concentrated up to a BVZ concentration of 3.2 mg/mL.

2.4. Preparation of BVZ-loaded tLyP-1 targeted HANAs

tLyP1 targeted non-PEGylated NPs (**tLyP1HA-NAs**) were prepared following an assembling technique previously described. Briefly, 125 μL of an aqueous solution of BVZ (16 mg/mL, stock concentration) were added to 500 μL of an hydroalcoholic solution of HAC16-tLyP1 (4 mg/mL, stock concentration) under magnetic stirring at 1100 rpm. Then, 50 μL of an ethanolic solution of Lipoid S100 (20 mg/mL, stock concentration) were added drop by drop over the HAC16-tLyP1/BVZ solution. Finally, the volume was made up to 1 mL with PBS.

tLyP1 targeted PEGylated NPs (**tLyP1PEG-NAs**) were developed as described in Section 2.3 with minor modifications. Thus, 125 μL of an aqueous solution of BVZ (4 mg/mL, stock concentration) were added over 500 μL of an hydroalcoholic solution of HAC16 30-70 kDa DS 1–10% (0.5 mg/mL, stock concentration), under magnetic stirring at 1100 rpm. Then, 50 μL of an ethanolic solution of Lipoid S10 (20 mg/mL, stock concentration) and DSPE.PEG$_{2K}$-tLyP1 (final concentration from 0.025 to 0.1 mg/mL) were added drop by drop over the HAC16/BVZ solution. Finally, the volume was made up to 1 mL with PBS.

Blank tLyP1-HANAs were prepared following the same procedure but replacing the mAb solution by ultrapure water.

HANAs were concentrated, removing the ethanol under a nitrogen stream up to a BVZ concentration of 3.2 mg/mL.

2.5. Preparation of antiKRAS^{G12V}-loaded tLyP-1 targeted HANAs

125 μL of an aqueous solution of antiKRAS^{G12V} mAb (4 mg/mL, stock concentration) was added to 500 μL of a 40% *v*/v of EtOH/ultrapure water solution of HAC16-tLyP1 (0.5 and 1 mg/mL, stock concentrations) under magnetic stirring at 1100 rpm. Then, 50 μL of an ethanolic solution of Lipoid S100 (from 5 to 10 mg/mL, stock concentrations) were added dropwise over the HAC16-tLyP1/antiKRAS^{G12V} mAb mixture. Finally, the volume was made up to 1 mL with PBS.

AntiKRAS^{G12V} mAb-loaded PEGtLyP1-HANAs were developed as follows, an aqueous solution of antiKRAS^{G12V} mAb (4 mg/mL, stock concentration) was added over 500 μL of HAC16 under magnetic stirring at 1100 rpm. Over it, 50 or 100 μL of a solution of Lipoid S100:DSPE.PEG$_{2k}$-tLyP1 were added dropwise over the HAC16/antiKRAS^{G12V} mAb mixture. Finally, the volume was made up with PBS until reaching a final formulation volume of 1 mL. HANAs were concentrated, removing the ethanol under a nitrogen stream. Prior to it, stocks solution of Lipoid S100 and DSPE.PEG$_{2k}$-tLyP1 were prepared in EtOH and 10% ultrapure water/ EtOH (*v*/v) at final concentrations of 20, and from 0.4 mg/mL, respectively. Then, equal volumes of each solution were mixed. For the polymer, HAC16 was dissolved in 40% v/v of EtOH/ultrapure water at 0.5 mg/mL.

Blank tLyP1-HANAs were prepared following the same procedure but replacing the mAb solution by ultrapure water.

Blank and antiKRAS^{G12V} mAb HANAs were concentrated, removing the ethanol under a nitrogen stream up to an antiKRAS^{G12V} mAb concentration of 3.2 mg/mL.

2.6. Physicochemical and morphological characterization

The physicochemical characteristics of the HANAs were determined by using a Malvern Zeta-Sizer (NanoZS, ZEN 3600, Malvern Instruments, Worcestershire, United Kingdom). For the analysis, HANAs were accordingly diluted in PBS and particle size, PDI and derived count rate (DCR) were determined using Dynamic Light Scattering (DLS). By using the same device, the zeta potential was recorded by Laser Doppler Anemometry (LDA) after measuring the mean electrophoretic mobility. For a further physicochemical characterization based on particle size and HANAs concentration, samples were analyzed by Nanoparticle Tracking Analysis (NTA) after diluting the samples in PBS (NanoSight NS3000, Amesbury, United Kingdom).

2D-cryogenic transmission electron microscopy (cryo-TEM) micrographs were collected on a 120 kV TEM equipped with an UltraScan 4000 SP cooled slow-scan CCD camera (GATAN) at x30,000 magnification. High quality data were collected on a JEM-2200FS/CR (JEOL, Ltd.) 200 kV TEM equipped with a K2 Summit direct detection camera (GATAN) at x30,000 magnification. To do so, sample preparation was performed using the Vitrobot Mark IV, applying 4 μL of HANAs (at 1:1 concentration) on a copper mesh. Vitrification was done in 70–80% humidity at RT. For quality control data was acquired on a JEM-1230 (JEOL, Ltd.)

2.7. Physicochemical and morphological characterization tLyP1-HANAs surface analysis by x-ray photoelectron spectroscopy (XPS)

Photoelectron spectra were acquired using A Thermofisher NEXSA spectrometer equipped with a hemispherical electron analyser and micro-focused monochromatic Aluminium Al Kα x-ray source (1486.6 eV). The samples were prepared pressing the sample powder on a double side conductive tape, and the tape attached to the instrument metal holder. The biggest x-ray spot of 400 μm was chosen by the operator. Residual vacuum in the analysis chamber was maintained at around 3×10^{-9} mbar. Data Analysis was performed with Avantage 6.7.0 Software, for elemental quantitation and peak fitting analysis. Intensities were estimated by calculating the area under peaks, after the subtraction of background. The used background is the “Smart background” based on the “Shirley background” with additional constraint that the background should not be of a greater intensity than the actual data at any point in the region. Experimental curve was fitted using a mix of Lorentzian-Gaussian lines in variable proportions. Binding energy was corrected and referenced respect the C1s component peak of aliphatic carbon at 284.8 eV after the peak fitting routine, following the ISO 19318:2004 procedure. A Flood gun (e- and Argon ions) was used to minimize surface charging. Binding energy of the aliphatic carbon C1s component peak was used as reference fixing its value to 284.8 eV. The correct surface charge compensation throughout the experiment was checked by acquiring the spectra of the Carbon C1s at the beginning and end of the experiment, the overlapping spectra practically indicate a correct charge stabilization and neutralization, and no chemical changes were observed due X-Ray irradiation.

The library applied is ALTHERMO1 (Modified Scofield) and use TPP-2 M method for attenuation length. This library was originally based on Scofield factors but with sensitivity factors adjusted based on experimental data acquired on Thermo fisher Scientific XPS instruments, with quantification over the main peak areas. Atomic ratios were computed from peak intensity ratios.

2.8. *Colloidal stability*

The colloidal stability of the HANAs was determined based on their physicochemical properties in simulated biological fluids and in suspension at 4 °C.

The stability in simulated biological fluids was evaluated upon incubation in PBS supplemented with 10% FBS after diluting the samples 10 times in the media. HANAs were incubated at 37 °C under orbital shaking at 300 rpm and, at different time points (0, 2, 4, and 8 h), 100 μL of the samples were withdrawn and both, particle size based on highest intensity peak and PDI were measured by DLS. As control, the HANAs were incubated in PBS and, the mean particle size and PDI were evaluated.

The stability of the HANAs in suspension at 4 °C was also evaluated. At the indicated time points, the particle size, PDI and zeta potential were determined as described in Section 2.6.

2.9. *Association efficiency (AE) and loading capacity (LC)*

HANAs were isolated by ultracentrifugation (*i.e.*, 35,000 rpm – 1.5 h – 15 °C) by using a Beckman Coulter (optime L90K) ultracentrifuge equipped with a Beckman type 70.1 Ti rotor. The amount of free BVZ or antiKRAS^{G12V} mAb in the supernatant was recovered and quantified.

BVZ association efficiency (AE %) to NPs was quantified using an enzyme-linked immunosorbent assay (ELISA). A 96-multiwell plate was coated with 0.005 μg antigen/well (*i.e.*, recombinant human VEGF$_{165}$) at a concentration of 0.05 μg/mL (100 μL/well) and incubated overnight at 4 °C. The antigen was prepared in coating buffer (1.59 mg/mL, Na_2CO_3, 2.94 mg/mL, $NaHCO_3$, pH 9.6). After the antigen attachment, the plate was washed four times with washing buffer (Tween 20 0.05% (*v*/v) in PBS, pH 7.4). The process was followed with a blocking step that was performed with 300 μL/well of blocking buffer (2% *v/w* of dry milk powder prepared in washing buffer) for 2 h at 37 °C under orbital shaking at 300 rpm. By the end, another washing step is done, and the antigen-coated plate is ready to use. Calibration curves for untreated BVZ and for the BVZ recovered from the supernatant were done by diluting accordingly and loading the samples on the previously prepared antigen-coated plate (incubation for 1 h at 37 °C). As control, a solution of BVZ at 3.2 mg/mL was treated in the same conditions and subsequently quantified. Then, the plate was submitted to a washing step with the addition of the secondary goat anti-human HRP antibody at a concentration of 0.08 μg/mL and incubated for 1 h at 37 °C. Finally, after this last washing step, the detection substrate (ABTS) was added (50 μL/well). After 25 min of incubation at RT, samples absorbances were measured at 405 nm by using a microplate reader (Synergy H4, BioTek, VT, USA).

The amount of associated antiKRAS^{G12V} mAb was determined by SDS-PAGE under reducing conditions. Briefly, the supernatant was diluted accordingly to fit in the calibration curve. AntiKRAS^{G12V} mAb standard solutions of known concentrations (from 2 to 0.2 μg/lane) were prepared in PBS. Treated samples were diluted in a volume ratio 1:1 with 2× Laemmli buffer and vortexed for several seconds. Then, samples were boiled at 99.5 °C for 5 min. 20 μL of the denatured samples were resolved using 12% polyacrylamide gels. After 1 h with variable milliamps and a 100–120 V voltage, the gel was fixed in 10% methanol and 7% acetic acid for 45 min. Finally, samples were stained using a SYPRO® Ruby protein gel stain solution overnight at RT. Prior to analysis, the gel was washed twice with ultrapure water. GelAnalyzer 19.1 software (www.gelanalyzer.com) by Istvan Lazar Jr., PhD and Istvan Lazar Sr., PhD, was used to process and analyze the samples. Total bands areas of the calibration curve were referred to the theoretical value and those ranging between 80 and 120% were considered. Samples' bands intensities referred to the calibration curve.

The AE and LC were determined as follows:

$$\text{AE } (\%) = [(\text{theoretical amount of mAb} - \text{free mAb}) / \text{theoretical amount of mAb}] \text{ x } 100$$

$$\text{LC } (\%) = [\text{associated mAb} / \text{total theoretical concentration of the HANAs}] \text{ x } 100$$

2.10. *Release profile*

BVZ or antiKRAS^{G12V} mAb released from the HANAs was quantified using ELISA and SDS-PAGE, respectively. Samples were diluted 10-times in PBS at pH 7.4 or pH 5.0 and incubated at 37 °C under orbital agitation (300 rpm). At different time points (0, 2, 4, 8, 24 and 168 h), the formulation was isolated by ultracentrifugation (35,000 rpm – 1.5 h – 15 °C). The free mAb in the supernatant was recovered and quantified by using the below equation where t_0 indicates the condition prior incubation, and t_1 corresponds to the condition at the time point of study.

$$\text{Cumulative mAb released } (\%) = \text{free mAb at } t_1 - \text{free mAb at } t_0$$

2.11. *Cell lines*

The lung adenocarcinoma human cell lines NCI-H441 (KRAS G12V) and NCI-H1568 (KRAS wild type) and murine cell lines A549 (KRASG12S) and CMT167 (KRAS G12V) were obtained from the American Type Culture Collection (ATCC). NCI-H441 and NCI-H1568 were grown in RPMI 1640, A549 and CMT167 in Dulbecco's Modified Eagle Medium (DMEM), all mediums supplemented with 10% FBS and penicillin/streptomycin, referred to as culture medium. All cells were routinely tested for mycoplasma infection.

2.12. Cytotoxicity studies of antiKRAS^{G12V} mAb-loaded HANAs

The lung cancer human NCI-H441, NCI-H1568 and murine cell lines A549 and CMT167 were plated in a 96-well plate at densities of 25 × 10^2 cell/well for the CMT167 cell line and 5 × 10^3 cell/well for the rest and incubated in 100 μL/well culture medium 10% of FBS at 37 °C. After 20 h of incubation, increasing concentrations of HANAs were resuspended in culture medium 5% FBS final concentration. After 24 h cell supernatant was discarded, and cells were incubated with alamarBlue, previously diluted in DMEM-10%FBS 100 μL/well. To evaluate the reduction of resazurin to resorufin as indicator of the mitochondrial respiratory chain in live cells, the resazurin was allowed to react for 40 min at 37 °C. Thus, resorufin levels were recorded at 544–590 nm by using a microplate reader (Synergy H4, BioTek, VT, USA). As positive control, cells were incubated in supplemented cell culture medium and considered as 100% of viability. Treated cells with Triton X-100 (0.5%, *v*/v in culture medium) were used as negative control, 0% of viability. Cell viability was calculated after subtracting negative control values to crude fluorescence values as follows:

$$\text{Cell viability }(\%) = [(\text{sample fluorescence} - \text{negative control fluorescence}) / \text{positive control fluorescence}] \text{ x } 100$$

2.13. AntiKRAS^{G12V} mAb antiproliferative activity

Cell proliferation studies were performed with cell lines NCI-H441 and NCI-H1568, and CMT167. Thus, an initial cell density of 5 × 10^3 NCI-H441 and NCI-H1568 cells/well and 2.5 × 10^3 CMT167 was seeded on a 24-well plate in culture medium supplemented with 5% of FBS. Cells were treated with free antiKRAS^{G12V} mAb and antiKRAS^{G12V} mAb-loaded HANAs at a 50 nM antiKRAS^{G12V} mAb concentration on days 1, 3 and 5 at 37 °C. Cells were exposed to blank HANAs at doses equivalent to the antiKRAS^{G12V} mAb. At days 1, 3, 5 and 7 a resazurin staining assay was performed. The medium was discarded and 400 μL/well of resazurin diluted in culture medium was added at the indicated time points. Resazurin was allowed to react for 40 min at 37 °C. Afterward, the medium was transferred to a 96-well plate and fluorescent levels were determined at 544–590 nm by using a microplate reader (Synergy H4, BioTek, VT, USA). Cells incubated in culture medium supplemented with 5% FBS was considered 100% viability. Aiming to compare cells growth over time, reads were referred to the cell viability at day 1 and considered 100%. When needed, reads were scaled up to a negative control well, Triton X-100 (0.5%, *v*/v in culture medium). The reduction of the cell proliferation at day 7 (%) was calculated by dividing the viability after the treatment with antiKRAS^{G12V} mAb-loaded HANAs by the viability after the treatment with the free antiKRAS^{G12V} mAb.

2.14. AntiKRAS^{G12V} mAb colony formation

The colony formation assay was performed by treating the CMT167 cells with the antiKRAS^{G12V} mAb-loaded PEGtLyP1-HANAs at a 100 nM antiKRAS^{G12V} mAb concentration. After 48 h, the cells were harvested and reseeded at 2 × 10^2 cells/well in a 6-well plate. Cells were treated with equivalent doses of blank PEGtLyP1-HANAs and used as control. They were allowed to growth for 7 days, after which they were washed once with PBS and prefixed with a solution of 50% culture medium, 37.5% methanol, and 12.5% acetic acid for 5 min. They were subsequently fixed for 10 min with methanol containing 25% acetic acid. The wells were then washed twice with PBS and stained with 0.05% crystal violet for 10 min. Three PBS washes were performed to remove the remaining staining. Colonies were counted and analyzed with ImageJ software. [29]

2.15. AntiKRAS^{G12V} mAb intracellular staining

The lung murine cell line CMT167 was seeded at densities of 25 × 10^3 cells/well in a 24-well plate in culture medium. After 24 h t, anti-KRAS^{G12V} mAb-loaded HANAs were diluted in DMEM (5% FBS final concentration) at a final antiKRAS^{G12V} mAb concentration of 1 μM. Equivalent antiKRAS^{G12V} mAb and blank NAs doses were added. After 4 h of incubation at 37 °C and 4 °C, incubation at 4 °C was performed to measure extracellular attachment or passive internalization since no active uptake occurs at this temperature, cells were rinsed 3 times with cold PBS detached with 100 μL/well of Accutase® at 37 °C. Once detached, cell suspension was collected in FACS tubes and washed with cold 3 mL of FACS washing buffer (PBS 2% FBS). Cells were centrifuged (1500 rpm, 5 min, 4 °C) and after discarding the supernatant, cells were fixed with 100 μL of paraformaldehyde (4%) for 30 min at RT followed by cell permeabilization and blocking achieved by 1 h incubation at 4 °C with PBS containing 0.3% Triton X-100 and 10% FBS. To detect the anti-KRAS antibody intracellularly, cells were incubated with F(ab')2-Goat anti-Mouse IgG (H + L) secondary antibody PE in PBS containing 0.3% Triton X-100 for 1 h at 4 °C. Between steps, unbound secondary antibodies were removed with 3 washes with PBS. Finally, cells were analyzed by flow cytometry in a FACSCalibur instrument (BD Biosciences, Franklin Lakes, NJ, USA). Percentage of intracellular anti-KRAS^{G12V} mAb was determined by the integrated mean fluorescence intensity (iMFI) calculated based on the % of positive cells with the MFI of that population.

2.16. Western blot analysis

CMT167 cells (0.5 × 10^5 cells/well) were plated in 6-well plates and treated with the PEGtLyP-1 HANAs at 37 °C for 48 h. After wash in cold TBS, cells were lysed in Pierce™ IP Lysis Buffer for 1 h at 4 °C. Nuclei and cell debris were removed by centrifugation at 8000 *g* for 15 min. Protein concentration was measured with the BCA protein assay reagent kit, following the manufacturer's instructions. To this end, 40–50 μg of protein from cell lysates were resolved in 12% SDS-polyacrylamide gels under reducing conditions and electrophoretically transferred to PVDF membrane. Afterwards, they were blocked with blocking buffer (1× TBS, 0.1% Tween-20 with 5% *w/v* nonfat dry milk) for 1 h at RT and incubated overnight at 4 °C with mAbs anti-phosphorylated-p44/42 MAPK (Erk1/2) (Thr202/Tyr204, Cell Signaling), anti-p44/42 MAPK (Erk1/2), anti-KRAS and anti-alpha tubulin B-7. The membranes were subsequently incubated for 60 min at RT with the appropriate fluorescently coupled secondary antibodies (anti-mouse DyLight™ 680 and anti-rabbit IgG DyLight™ 800) diluted in blocking buffer. Three 15-min washes between steps were performed with TBS-0.01% Tween 20. Bound Ab was detected with an Odyssey Infrared Imager, and densitometric analysis was performed using the Image Studio Little software (LI-COR Biosciences, Lincoln, NE, USA).

2.17. Target engagement

Target engagement studies were performed in the lung murine CMT167 cell line at densities of 0.5 × 10^5 cells/well plated in a 6-well plate. Cells were treated with HANAs at 50 nM of mAb. After 24, 48, or 72 h, cells were washed twice with PBS, and centrifuged at 1500 rpm 5 min. Then, the cell pellet was incubated with Pierce™ IP Lysis Buffer for 30 min at 4 °C. To pull down the mAb, 1 mg of total protein (carrying a theoretical amount of 20 μg of mAb) was immunoprecipitated for 1 h with 40 μL of Protein G PLUS-agarose beads at 4 °C in head-to-tail rotation. For positive target engagement control, 1 mg of CMT 167 cell lysate was incubated for 4 h at 4 °C (head-to-tail rotation) with 5 μg of free antiKRAS^{G12V} mAb and then immunoprecipitated as previously mentioned.

Samples were loaded in 12%-acrylamide PAGE gels and transferred to a PVDF protein blotting membrane. Membranes were incubated with antiKRAS mAb produced in mice followed by an anti-mouse IgG DyLight™ 680 antibody produced in goat. Finally, membranes were scanned using the LI-COR Odyssey Scanner system, and band intensities were quantified with LI-COR Image Studio™ Lite Quantification Software (LI-COR Biosciences, Lincoln, NE, USA).

2.18. *In vivo antitumor efficacy*

Female NMRI-Foxn1 nu/nu mice (6–8 weeks old) were purchased from Janvier Labs (Le Genest-Saint-Isle, France). 3×10^6 CFPAC-1 cells were subcutaneously injected in the right flank (200 μL of cell suspension in a 1:1 matrigel:PBS mixture). When tumors reached approximately 100 mm3 animals were allocated into the different experimental groups (6–8 animals per group) with equal tumor size distribution (average and variance): one group received antiKRA^{SG12V}-PEGtLyP1-HANAs at antiKRAS^{G12V} dose of 10 mg/kg, other group received the respective amount of blank-HANAs and a third group, used as control, was injected only with PBS. Treatments were administered intravenously twice a week. Tumor size was measured twice a week in two dimensions using a caliper, and the volume was expressed in mm3 using the formula Tumor Volume = width2 × length × 0.5. Animals were observed daily for clinical signs of pain or discomfort and weighted weekly.

All experimental procedures involving mice in this study were favorably evaluated by the institutional USC Bioethics Committee and approved by the Autonomous Government of Galicia (project ID 15012/2023/007), in accordance with European and Spanish legislation. Mice were housed at the Centro de Biomedicina Experimental (CEBEGA) animal facility in individually ventilated cages under SPF conditions, where they had *ad libitum* access to food (regular rodent chow) and water.

2.19. *Statistical analysis*

The statistical analysis was performed by fixing the confidence level at 0.05 and significant differences were considered for $^*p < 0.05$, $^{**}p < 0.01$, $^{***}p < 0.001$, and $^{****}p < 0.0001$. GraphPad Prism version 9.3.0 was the software of selection for the data analysis.

3. Results and discussion

Despite the recognized need of improving the intracellular delivery of mAbs in the context of cancer, the potential of nanotechnology for achieving this goal has hardly been explored. [30,31] This idea come to our mind a decade ago and, since then, we have developed different delivery platforms particularly adapted for fulfilling this unmet need. In fact, we were the first to disclose the *in vivo* performance of a nanocapsule delivery platform to confront critically relevant targets such as the gasdermine target [21] or the KRAS target. [32–34] Here, we disclose an additional effort to formulate the mAb anti-KRAS in the form of nanoassemblies exhibiting distinct and unusual properties. For example, they exhibit an unusual loading capacity in a special architectural organization. This was achieved thanks to the rational selection of hydrophobically modified hyaluronic acid (HA) in combination with phospholipids. We adapted the HANAs technology, previously developed for entrapping the clinically relevant mAb BVZ, [25] for the intracellular delivery of the antiKRAS^{G12V} mAb. Prior to it, we have functionalized the BVZ-loaded HANAs with the tLyP1 peptide to maximize the tumor accumulation chances and validate them for the anti-KRAS^{G12V} mAb. An essential step was to assess the capacity of the HANAs to enter the cells and to deliver the anti-KRAS cargo at the intracellular level, ensuring the adequate engagement of the KRAS^{G12V} oncoprotein. Finally, the therapeutic efficacy was investigated a pancreatic ductal adenocarcinoma tumor model.

3.1. *Engineering a synthetic procedure for the tLyP1 functionalization of HAC16 and DSPE.PEG$_{2K}$*

To develop tLyP1-targeted HANAs, we selected two components known for their efficient integration onto the NP surface, hypothesis further motivated by the formulation method employed. Additionally, the confirmation of core-shell nanostructures in the BVZ-loaded HANAs, characterized by a hydrophilic core encased within a bilayer, indicates the surface disposition of the hydrophilic components. [25] Consequently, our investigation focused on the functionalization of two integral components: HAC16 and DSPE.PEG$_{2K}$.

To ensure the obtention of a pure conjugate while preserving the original physicochemical properties of the NPs, several optimizations of the synthesis and formulation conditions were conducted.

For the functionalization of the HAC16, a two-steps reaction consisting of a carbodiimide followed by a maleimide reaction chemistry was conducted. The presence of carboxylic groups in the polysaccharide structure enabled their amidation with maleimide groups. Consequently, this condition allows an effective conjugation *via* the thiol groups of the selected peptide with the double bond of the polymer-maleimide derivative, building the thio-succinimide link. In the case of DSPE-PEG$_{2K}$, we adapted the reactions conditions described in the literature, [12,35] which simply involves the thiol-maleimide reaction. Under these reaction conditions, polymers and lipids can be functionalized *via* a simple and reproducible method. The use of mild conditions ensures the preservation of the biological functionality.

The amphiphilic polymer HAC16 MW 30–70 kDa DS 1–10% was functionalized following the above-described two-steps reaction. Following an extensive screening of different molar ratios of carboxylate groups, carbodiimide, N-hydroxysuccinimide, maleimide, and tLyp1 (COOH:EDC:NHS:Mal:tLyp1), the ratio 1:0.164:0.327:0.327 was selected and characterized by ^{1}H NMR (Suppl. Fig. 1). The successful incorporation of the tLyP1 was confirmed by the correlation of the methyl group of the *N*-acetyl group (-CO-CH3) at δ 2.0 ppm with the α-proton from the 7th arginine (-CH-(CH2)3-NHC(=NH)NH2) at δ 4.2 ppm **(**Fig. 1A**).** The successful conjugation was further supported by the disappearance of vinyl protons signal of the maleimide at δ 7.0 ppm. Hence, the integration of the tLyP1 signal with the signal that corresponds to the HAC16 yielded a degree of substitution (DS) of the HAC16-tLyP1 conjugate of 2.1 (%) ± 0.9.

The versatility of this reaction for other polymers was confirmed in a HAC16 polymer with superior amount of C16 aliphatic chains (HAC16 MW 30–70 kDa DS 10–15%), yielding values comparable to the previous polymer (DS of 4.3 (%) ± 1.0, $n = 3$).

For the DSPE.PEG$_{2k}$-tLyP1 conjugation, a thiol-maleimide reaction was carried out **(**Fig. 1B) and characterized by H-NMR (Suppl. Fig. 2). The disappearance of the maleimide singlet peak at 7.0 ppm was used as an indicator of the coupling. Lastly, the covalent conjugation was verified by comparison of the integral of the peak corresponding to the methyl groups (6H) of the DSPE (δ 0.85 ppm) with the methyl group (3H) of the tLyP1 threonine (-CHOH-CH$_3$) at δ 1.05 ppm. As a result, a DS (%) of 94.8 ± 12 was reached ($n = 4$), suggesting the absence of non-functionalized DSPE.PEG$_{2k}$-mal products.

3.2. *Development and characterization of bevacizumab-loaded tLyP1-targeted HANAs with tunable properties*

HANAs were prepared by the assembling technique previously described by our group, [25] exhibiting interesting features that make them attractive as mAb-delivery systems for cancer therapy. The above synthetized tLyP1-conjugates were employed for the surface

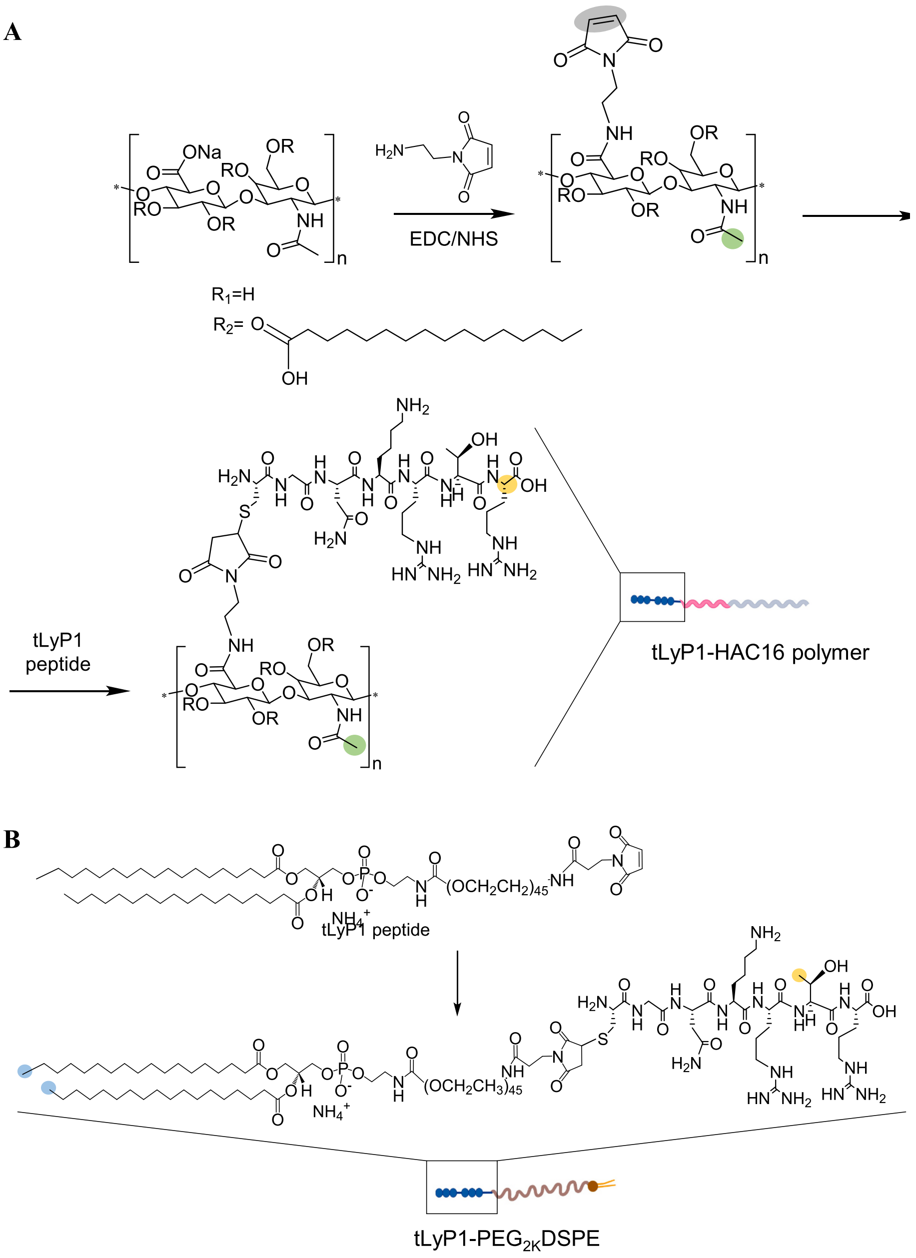

Fig. 1. Functionalization approach of tLyP1-conjugates. Representative illustration of the stepwise chemical evolution from **(A)** HAC16 to HAC16-Maleimide and HAC16-tLyP1 conjugate and **(B)** from DSPE.PEG$_{2K}$ to DSPE.PEG$_{2K}$-tLyP1. Dots in the HAC16 reaction: grey indicates the singlet (2H) from the double bond of the maleimide and yellow denotes the triplet (1H) of the arginine alpha-hydrogen proton of the peptide. Dots in the DSPE.PEG$_{2K}$ reaction: blue represents the singlet (3H) from the methyl groups of the methyl group of the *N*-acetyl group (-COCH3) of HAC16 and yellow the methyl group (3H) of the tLyP1 threonine (-CHOH-CH3) of the peptide. EDC 1-ethyl-3-(−3-dimethylaminopropyl) carbodiimide hydrochloride; NHS N-hydroxysuccinimide. (For interpretation of the references to colour in this figure legend, the reader is referred to the web version of this article.)

functionalization of the BVZ-loaded HANAs. The functionalization approach and the physicochemical properties of the resulting tLyP1-targeted HANAs are summarized in Table 1 and compared with the non-targeted counterpart.

For the functionalization of non-PEGylated HANAs (**HA-NAs**), native HAC16 was shifted by the tLyP1-HAC16 conjugate while the amount of each component was maintained. As observed, the physicochemical properties of the resulting tLyP1-targeted HANAs (**tLyP1HA-NAs**) were similar to those of the non-targeted counterpart. The resulting **tLyP1HA-NAs** exhibited a size of around 167 nm and a neutral surface charge. Moreover, the tLyP1 incorporation dropped the AE (%), from 86 to 26. We speculate that since the addition of the hydrophilic tLyP1 induces changes in the physical properties (*i.e.*, solubility) of the tLyP1-HAC16, it is expected to observe structural changes in the NPs and thus, a reduction in the AE.

In the case of the PEGylated HANAs (**PEG-NAs**), the incorporation of increasing concentrations of DSPE.PEGtLyP1 conjugates revealed a direct correlation with the particle size (**see** Suppl. Fig. 3). These led us to the selection of the **tLyP1PEG-NAs** with the lowest concentration tested (0.01 mg/mL), aiming to preserve a particle size of around 100 nm, [36–38] desirable feature for the NPs access and accumulation into the tumor tissue. Hence, the resulting monodisperse **tLyP1PEG-NAs** exhibited a size of around 120 nm with neutral surface charge. Unlike the aforementioned observation, the tLyP1 functionalization approach did not compromise the AE, which remained at 65%. The low proportion (~1%) that the DSPE.PEG-tLyP1 represents over the total system may be

Table 1
Physicochemical properties, AE, and LC of the tLyP1-functionalized HANAs at a final BVZ concentration of 3.2 mg/mL in comparison with the non-functionalized counterparts. Data are expressed as mean ± SD, $n \geq 3$. N.A. not applicable, AE association efficiency, LC loading capacity.

BVZ-loaded HANAs	Functionalization approach	Physicochemical properties			AE (%)	LC (%)
		Particle size (nm)	PDI	Zeta potential (mV)		
HA-NAs	N.A.	162 ± 17	0.23	−13 ± 2	86 ± 11	34.4
tLyP1HA-NAs	HAC16	166 ± 9	0.18	−11 ± 6	26 ± 11	10.3
PEG-NAs	N.A.	79 ± 8	0.25	−13 ± 2	67 ± 21	22.2
tLyP1PEG-NAs	PEG	121 ± 14	0.25	−13 ± 2	65 ± 12	26.0

the responsible for this outcome. Importantly, it is noteworthy that the LC values exceeding 25% surpass those reported for mAbs delivery systems. [39,40]

The size distribution of both BVZ-loaded tLyP1-HANAs was further confirmed by NTA, as displayed in Fig. 2.

3.2.1. *Colloidal stability*

3.2.1.1. Stability examination in simulated biological media. tLyP1-HANAs were incubated upon incubation in PBS-10%FBS and PBS at 37 °C overtime (Fig. 3A). Hence, HANAs exhibited an increment in the particle size upon incubation in the rich protein media, followed by a particle size stabilization comparable to the NPs in PBS. We attributed this behavior to the high affinity of the FBS proteins for the NPs surface, which is governed by NPs composition. Overall, these results confirmed the favorable behavior of the NPs in *in vivo* conditions as they demonstrated high stability in simulated conditions for at least 8 h.

3.2.1.2. Long-term storage in suspension and freeze-drying preserve the HANAs properties. A key feature of biopharmaceutical products is their stability during storage in suspension. Therefore, NPs were stored at 4 °C and the colloidal stability was evaluated overtime. Results in Fig. 3B demonstrated the long-term stability of HAtLyP1 and PEGtLyP1 for at least 6 months in terms of particle size, PDI and surface charge.

On the other hand, the possibility of storing the HANAs in powder form was explored (Fig. 3C). To find the most suitable condition, HAtLyP1 and PEGtLyP1 were freeze-dried in the presence trehalose at 2.5 and 5% (*w/v*). The results of the screening led to the selection of trehalose 5% for both HANAs, since the original physicochemical properties and the amount of entrapped BVZ to the HANAs after resuspension were guaranteed.

3.2.2. *Release profile*

The *in vivo* outcome of nanocarriers maybe governed by their controlled release dynamics during their circulation in the blood stream and, subsequently, in the TME. In the case of HANAs, it could be presumed that the mAb is gradually released within the extracellular and intracellular compartments of the tumor tissue. Hence, the study the mAb release kinetics from tLyP1-targeted HANAs was conducted at pH 7.4 and 5.0 in an attempt to simulate both environments. The results in Fig. 3D indicate that the release profiles were similar at both pH values, however, the burst effect, which was slightly superior for the functionalized nanocarriers. This might be due to the greater hydration of the lipid bilayer ascribed to the presence of PEG, [41] which may interfere with the architecture of the system, triggering the release of the mAb. Overall, the singularity of the release profile relies on the limited release over the time, a fact that could be attributed to the robust interactions observed among the components of HANAs and the mAb, as previously suggested. [25] We posit that more disruptive conditions, such as a rich enzymatic environment, will induce the mAb release. For instance, the degradation of the HA polymer by hyaluronidases [42], as well as the presence of phospholipase A2 enzymes [43,44] are expected to trigger the degradation of the nanocarrier's components, leading to the release of the mAb in the cytosol.

In brief, the HANAs technology functionalized with the tumor penetrating peptide, tLyP1, maintains its capacity to entrap the BVZ, its colloidal stability in several simulated media and the slow released profile.

3.3. *Development and characterization of antiKRAS^{G12V} mAb-loaded tLyP1-targeted HANAs*

Given the potential of the HANAs technology, we decided to evaluate

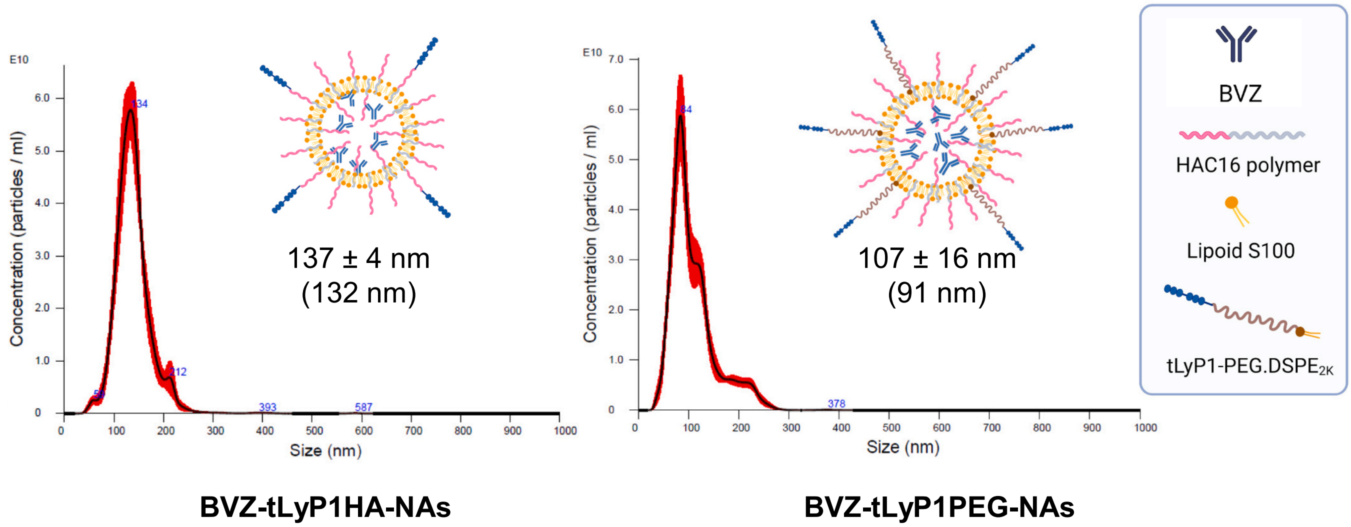

Fig. 2. Characterization of BVZ-loaded tLyP1HA-NAs and tLyP1PEG-NAs. Graph distribution of BVZ-loaded tLyP1HA-HANAs (left graph) and BVZ-loaded tLyP1PEG-NAs (right graph) by NTA. Data are expressed as mean ± SD, $n \geq 3$.

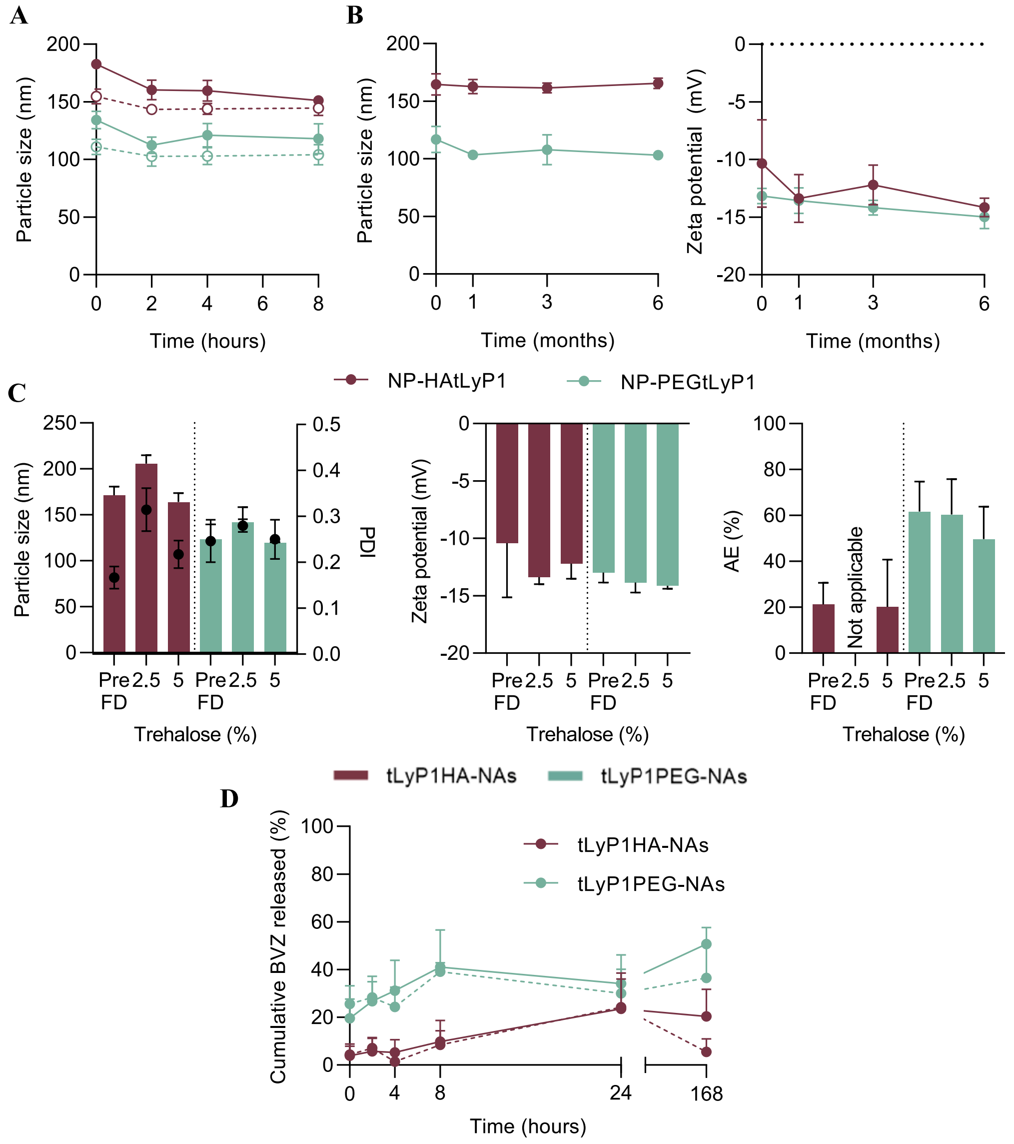

Fig. 3. Characterization of BVZ-loaded tLyP1-targeted HA-NAs and PEG-NAs. **A.** Stability in simulated biological fluids of upon incubation at 37 °C. Particle size evolution in PBS supplemented with 10% FBS (fill dots) and PBS (empty dots). Mean ± SD, *n* = 3. **B.** Long-term stability based on particle size and Zeta potential upon storage in suspension at 4 °C for up to 6 months. Mean ± SD, n ≥ 3. **C.** Physicochemical characterization and AE (%) before and after freeze-drying in the presence of trehalose (%, *w/v*). Mean ± SD, n ≥ 3. **D.** Release profile of upon incubation in PBS pH 7.4 and 5.0 at 37 °C. Dashed and continuous lines indicate the cumulative BVZ released at pH 5.0 and 7.4, respectively. Data are represented as mean ± SEM, n ≥ 3. AE association efficiency.

its therapeutic potential for the challenging therapeutic oncoprotein, KRAS^{G12V}. Building on the conclusions derived from the above studies regarding the structural changes that the presence of tLyP1 induces and aiming to maximize the changes of tumor accumulation, we adapted the aforementioned BVZ-loaded tLyP1HA-NAs and BVZ-loaded tLyP1PEG-NAs for the entrapment of the antiKRAS^{G12V} mAb. Through it, the advantages of the functionalization approach, whether through the HA or the PEG, will be explored. In alignment with the optimization, a targeted particle size of approximately 100 nm was pursued [36–38], aiming to enhance accessibility and accumulation within tumor tissues.

To establish the optimal formulation conditions for the entrapment of the antiKRAS^{G12V} mAb, we fixed the initial concentration of mAb at 0.5 mg/mL and investigated the influence of the concentrations of HAC16-tLyP1 (0.25 and 0.5 mg/mL) and Lipoid S100 (0.25, 0.5 and 1 mg/mL) in a volume ratio HAC16/antiKRAS^{G12V} mAb /Lipoid S100 of 10:2.5:1, and the resulted HANAs were studied in regards to their particle size. Results in Suppl. Fig. 4 indicate that, irrespectively of the lipid, increasing concentrations of HAC16-tLyP1 led to an increment in the particle size, with sizes remaining below 200 nm. These results suggest the role played by the polymer and therefore, the hydrophobic interactions, in the HANAs assembly. The prototype, initially comprising HAC16-tLyP1 0.25, Lipoid S100 1, antiKRAS^{G12V} mAb 0.5 (mg/mL), exhibited the smallest particle size (~130 nm) and therefore, was selected for further studies, from now on designated as **antiKRAS^{G12V} mAb -tLyP1-NAs.**

Table 2
Physicochemical properties by DLS, AE (%) and LC (%) of antiKRAS^{G12V} mAb tLyP1-NAs and PEGtLyP1-NAs at a mAb concentration of 3.2 mg/mL. Data are expressed as mean ± SD, *n* ≥ 3. AE association efficiency, LC loading capacity.

antiKRAS^{G12V} mAb -HANAs	Particle size (nm)	PDI	Zeta potential (mV)	AE (%)	LC (%)
tLyP1-NAs	141 ± 7	0.20	−11 ± 2	66 ± 9	18.7
PEGtLyP1-NAs	142 ± 11	0.23	−11 ± 2	64 ± 6	18.2

To further expand the properties of HANAs, they were granted with a stealth corona through the incorporation of PEG to the NPs' surface. Thus, a DSPE.PEG$_{2K}$-tLyP1 final concentration of 0.01 mg/mL was introduced to the above system without modifying its physicochemical properties. Indeed, monodisperse NPs with a particle size of 150 nm and neutral surface charge were obtained. This candidate was so-called **antiKRAS^{G12V} mAb -PEGtLyP1-NAs**.

Selected lead candidates (antiKRAS^{G12V} mAb-tLyP1-NAs and antiKRAS^{G12V} mAb-PEGtLyP1-NAs) were submitted to a concentration process to achieve clinical doses and further characterized. Table 2 summarized the physicochemical properties, depicting reproduceable NPs with the desired particle size (~140 nm) and neutral surface charge. In good agreement, mean values acquired by NTA confirmed the monodispersity and particle size of antiKRAS^{G12V} mAb-HANAs (**Fig. 4**). As control, blank NPs were produced and characterized (**see** Suppl. Table 1).

Following the development process, the most promising candidates were selected for assessing their capacity to entrap the antiKRAS^{G12V} mAb. Consequently, AE values of 60% were exceeded for both prototypes, with noteworthy LCs reaching ~18.7%. Notably, contrary to prior findings, [45] the incorporation of a PEGylated lipid did not influence the physicochemical properties or LC of the HANAs. This discrepancy may be related to the low proportion (~1%) that the DSPE.PEG-tLyP1 represents over the total system. Despite this, the attained high LC values, notably surpassing those reported for mAbs delivery systems, are noteworthy. Such stable and elevated LC values are indicative of a favorable safety profile, desirable attributes for emerging biopharmaceutical products. It can be postulated that the formulation method and the limited quantity of components utilized are pivotal factors contributing to the observed AE, aligning with our earlier hypothesis.

3.3.1. Morphological and surface characterization by cryo-TEM and X-ray photoelectron spectroscopy (XPS)

To delineate the native morphology of the HANAs, blank and antiKRASG12V mAb PEGtLyP1-NAs were subjected to cryo-TEM (**Fig. 5A**). In terms of structural organization, the acquired 2D cryo-images show the presence of unilamellar or multilamellar vesicular structures consisting of a lipid/polymer bilayer and an aqueous core. Notably, in the experimental set-up used, no striking differences, were observed among blank and loaded NPs, indicating minimal impact of the mAb incorporation onto the structural arrangement of the system. Morphologically, the images unravelled heterogeneous populations that falls into spherical to oval shape and particle sizes <100 nm, consistent with the particle size obtained from above orthogonal sizing techniques. Overall, on the basis of the structural analysis, we could infer a population of bilayer polymer/lipid assemblies, [46,47] alongside some irregular undefined nanoaggregates. These undefined nanostructures might be due to the complexation of the mAb with the polymer (HAC16) and/or the lipid (Lipoid S100).

XPS is a surface-sensitive technique providing information about the elemental composition of <10 nm thick surface layer. Herein, XPS was performed in "as received" condition, operating in spectroscopic mode, to provide an insight on the distribution of the components of the tLyP1-PEGNAs on its surface (**Fig. 5B**). This study was performed for blank tLyP1-PEGNAs in order to avoid possible interferences of the mAb elemental composition. Hence, the presence of lipids on the surface of the HANAs has been conclusively confirmed through the detection of P2p signals. Elemental composition analysis reveals comparable levels of phosphorus in the control lipid and tLyP1-PEGNAs, albeit in lower proportions in the polymer control. XPS elemental composition analysis further corroborates the presence of phosphorus in expected proportions, likely originating from the Lipoid S100 disposition on the surface of the HANAs. The anticipated presence of phosphate (PO4)-3 groups in the control lipid, a key constituent of phospholipids, is consistent with findings. Concomitantly, the presence of the HAC16 polymer on the surface of the tLyP1-PEGNAs was confirmed through N1s signals. In the control lipid, the N1s signal presents a single peak, indicative of one chemical environment, centred at 402.5 eV with 100% relative intensity. Conversely, the N1s signal of the polymer displays two chemical environments. The primary peak, centred at 399.8 eV with 91.66% relative intensity, predominates, while a secondary peak appears at a higher binding energy of 402.6 eV with 8.34% relative intensity, similar to that observed in control lipid.

These results allow us to conclude the surface disposition of both the polymer and the lipid, Lipoid S100. This, together with the nature of the components, it is highly likely that the hydrophilic segment of the components (*i.e.*, HA segment from HAC16 and phosphatidylcholine from Lipoid S100) are the ones found in the outer surface. Additionally, previous hypotheses suggesting the exposure of tLyP1 to the outer NP environment following its conjugation to the lipid or polymer are supported.

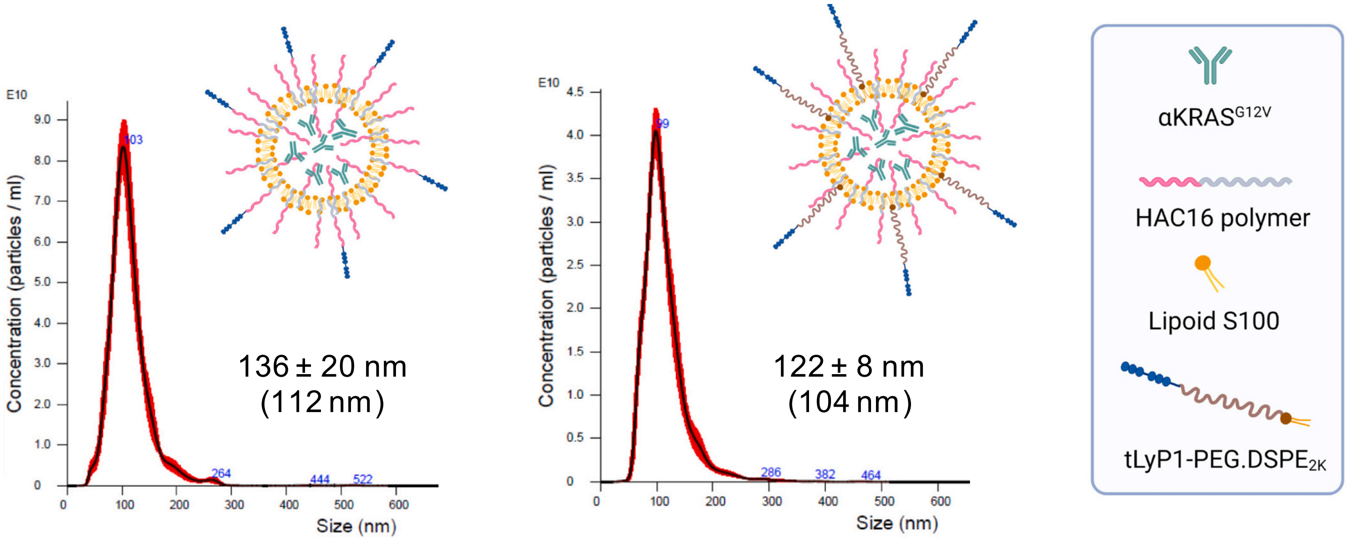

αKRAS^{G12V} tLyP1-NAs   **αKRAS^{G12V} tLyP1-PEGNAs**

Fig. 4. Schematic representation of the tLyP1-NAs and PEGtLyP1-NAs entrapping the antiKRAS^{G12V} mAb, its composition and the particle size distribution by NTA.

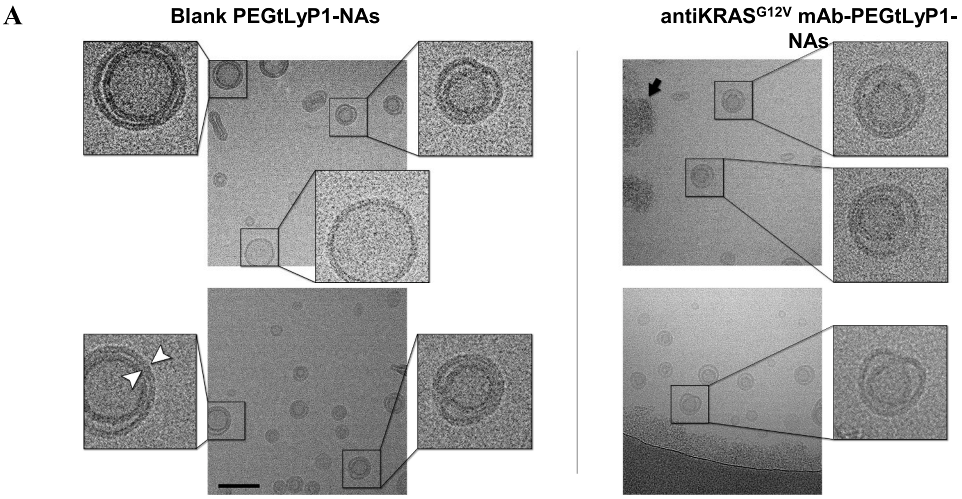

B

Name	Binding energy (eV)	Relative %
Lipoid S100		
N1s A	402.5	100%: R4-N+ Quaternary ammonium
HAC16 polymer		
N1s A	399.8	91.66%: (C=O)-CH-C Amide
N1s B	402.6	8.34%: R4-N+ Quaternary ammonium
Blank PEGtLyP1-NAs		
N1s A	399.4	38.93: C-NH$_2$ Amine
N1s B	402.4	61.07: R4-N+ Quaternary ammonium

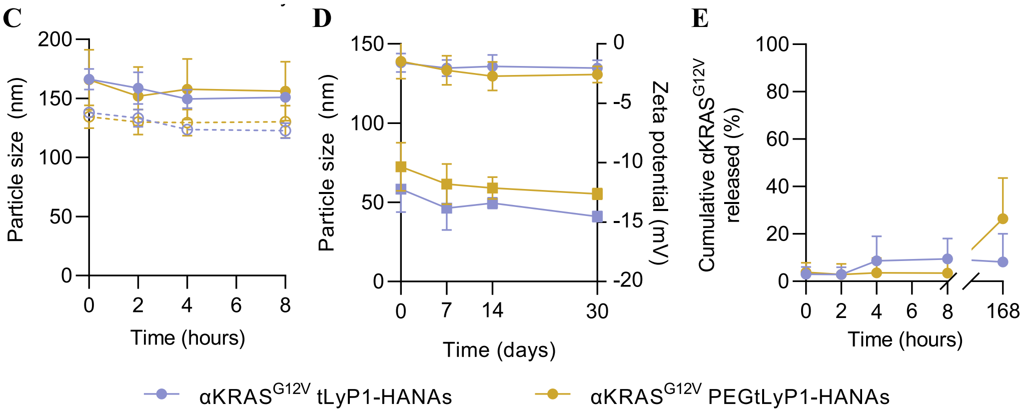

Fig. 5. Characterization PEGtLyP1-NAs and tLyP1-NAs for αKRAS^{G12V} delivery. **A.** Gallery of cryo-TEM micrographs. Cryo-TEM micrographs of blank and αKRASG12V PEGtLyP1-NAs. Scale bar 100 nm, inset x3 enlarged from original; white arrowheads mark the ~3.5 nm thickness of the bilayer, the black-arrow presence of nanoaggregates. **B.** XPS Binding Energies and Relative Percent of N1s species of the free polymer and Lipoid S100, and the respective PEGtLyP1-NAs. "A" and "B" indicate the chemical environments or species that are detected in the Nitrogen of each sample. **C.** Stability of αKRAS^{G12V} tLyP1-NAs and αKRAS^{G12V} PEGtLyP1-NAs upon incubation in relevant biological media at 37 °C. Mean particle size in PBS and particle size by intensity in PBS-10%FBS were recorded overtime. **(d)** Long-term stability based on particle size (circle) and Zeta potential (square) upon storage in suspension at 4 °C for up to 30 days. **(e)** Cumulative % of released αKRAS^{G12V} from tLyP1-NAs and PEGtLyP1-NAs quantified by SDS-PAGE. HANAs were incubated in PBS pH 7.4 at 37 °C for up to 1 week. Data are expressed as mean ± SD, n ≥ 3. FWHM full width at half maximum.

3.3.2. Colloidal stability in simulated biological media and under storage conditions

We studied the colloidal stability of selected HANA prototypes upon incubation at 37 °C in a relevant biological media (*i.e.*, PBS supplemented with 10% of FBS) and PBS as control. As shown in Fig. 5C, the particle size of tLyP1-HANAs was found to be stable upon incubation in biorelevant media for up to 8 h. These results indicate that the interaction of the components forming the assembly, presumably hydrophobic and ionic forces as observed for other mAbs, is strong enough as to prevent any premature degradation of the HANAs.

Performing preliminary storage stability studies is critical to ensure the adequate use of the HANAs and to anticipate stability issues in the potential preclinical development of the prototypes. Therefore, the stability in suspension at 4 °C of the HANAs was investigated overtime (Fig. 5D). The long-term stability in terms of particle size, PDI and surface charge was confirmed, which was found to be of at least 30 days.

3.3.3. Release profile

A recurring challenge in formulating biopharmaceuticals lies in the premature release during circulation, [48,49] particularly problematic for mAbs addressing intracellular targets where off-target accumulation compromises the therapeutic effect. In order to ensure the capacity of the HANAs to retain the mAb during blood circulation, we quantified the amount of antiKRAS^{G12V} mAb released from the HANAs after incubation in PBS pH 7.4 at 37 °C (Fig. 5E). Both prototypes, independently of the functionalization approach show the same release profile, characterized by a very slow release, reaching ~26% after 1 week of incubation. The absence of burst release is a consequence of the important interaction of antiKRAS^{G12V} mAb with the components of the HANAs.

These findings suggest that antiKRAS^{G12V} mAb molecules would not be prematurely released during plasma circulation and subsequent biodistribution. As stated before, more disruptive conditions, such as a rich enzymatic environment, will induce the mAb release.

The aforementioned findings underscore the versatility of HANAs technology in terms of its functionalization with the tumor penetrating peptide, tLyP1 and its capacity to entrap different mAbs. Hence, we anticipate the applicability of the technology for the entrapment of other mAbs and the functionalization with other targeting ligands. To identify the most promising candidate, we evaluated the ability of the anti-KRAS^{G12V} mAb -loaded HANAs to interfere with the cell signaling and growth, as well as capacity to engage the KRAS^{G12V} oncoprotein.

3.4. antiKRAS^{G12V} mAb-loaded HANAs impairs KRAS-mutant cell signaling and growth

The functional activity of antiKRAS^{G12V} mAb -loaded HANAs was

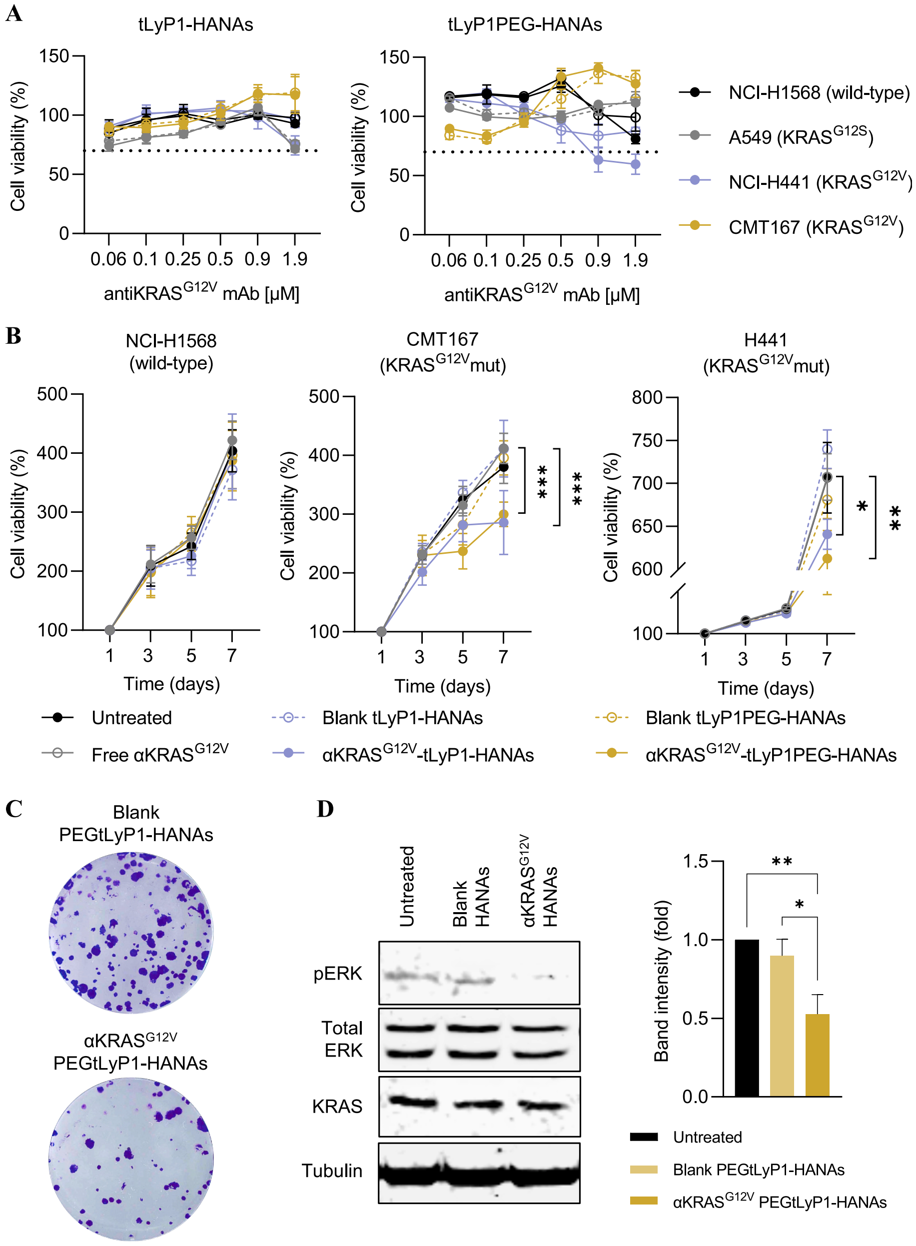

Fig. 6. Functional evaluation of αKRAS^{G12V}-loaded tLyP1-NAs in several lung cancer cell lines. **A.** Cell viability of lung cancer cell lines treated with blank (open dots) αKRAS^{G12V}-HANAs (filled dots) after 24 h of exposure. An αKRAS^{G12V} concentration of 1.9 µM corresponds to 0.7 mg/mL of HANAs. Cell viability values below 70% were considered toxic (dashed lines). Data are presented as viability percentage setting the control group (untreated cells) to 100%. **B.** αKRAS^{G12V} -HANAs impaired G12V mutated lung cancer cell proliferation. Statistical differences between free αKRAS^{G12V} and other treatments were analyzed by 2-way ANOVA followed by a Fisher's LSD test. Differences at 5 days were not plotted. **C.** Inhibition of tumor colony formation by αKRAS^{G12V}-PEGtLyP1-NAs. **D.** Western blot analysis and pERK/total ERK downregulation after treatment with αKRAS^{G12V}-PEGtLyP1-NAs in CMT167. Densitometric analysis was used to evaluate the reduction of pERK staining intensity in respect to total ERK and determined to be statistically significant using one-way ANOVA followed by a Fisher's LSD test. Tubulin is used as the housekeeping protein expression control. Data are expressed as mean ± SEM, n ≥ 3.

evaluated across a panel of cell lines: NCI-H1568 (wild-type), A549 (KRAS^{G12S}-mutant), CMT167 and NCI-H441 (KRAS^{G12V}-mutants). In cell viability assays, the two leading candidates (antiKRAS^{G12V} mAb-tLyP1-NAs and antiKRAS^{G12V} mAb-PEGtLyP1-NAs) were tested at increasing concentrations of (60–1900 nM) antiKRAS^{G12V} mAb (Fig. 6A). As displayed, antiKRAS^{G12V} mAb -loaded PEGtLyP1-NAs impaired the growth in the KRAS^{G12V}-mutant NCI-H441 cell line but not in CMT167. These observations, coupled with the absence of activity observed from KRAS^{G12S}-mutant, wild-type cell lines and blank HANAs, implies a specific cell line-dependent activity elicited by the intracellular delivery of the mAb. [50,51] Hence, the specific activity associated to the antiKRAS^{G12V} mAb was suggested while the low cytotoxicity profile of the HANAs was confirmed.

RAS mutations are implicated in cell proliferation [3,5] and colony formation, an outcome advocated by the persistent activation of the RAS protein. Consequently, the efficacy of the antiKRAS^{G12V} mAb in diminishing the number of proliferating cells through its entrapment into the HANAs was assessed over 7 days (Fig. 6B). Upon evaluating the activity of the antiKRAS^{G12V} mAb -tLyP1-NAs in KRAS^{G12V}-mutant cell lines (NCI-H441 and CMT167), a suppression of the proliferation was observed, with rates of 9% and 36%, respectively. Consistent with these findings, PEGtLyP1-NAs exhibited a comparable delay in cell proliferation, which was of 27% (CMT167) and 19% (NCI-H441) with statistically significant differences even on day 5 of treatment. The superior rate of response observed in the CMT167 cell line might be attributed to a high expression of the tLyP1 receptor, NRP-1 [26,27] or the absence of resistance mechanisms, [52–54] a phenomenon documented in other KRAS-mutant cell lines where KRAS knockdown activated downstream pathways, including ERK and AKT. [51,55] Despite, since absence of activity was displayed with control groups (untreated cells, free mAb, or blank HANAs) and in the wild-type cell line, the specific activity ascribes to the antiKRAS^{G12V} mAb triggered by the HANAs was confirmed. These variable inhibition levels observed among HANAs and cell lines are consistent with prior *in vitro* studies on KRAS siRNA-based therapeutics. [56,57] In parallel, the oncogenic effects of the most efficacious candidate (antiKRAS^{G12V} mAb-PEGtLyP1-NAs) was further evaluated by clonogenic studies. As displayed in Fig. 6C, the relative degree of inhibition in the oncogenic KRAS^{G12V} mutant cell line CMT167 was 36 (%) ± 11.

KRAS-mutated cancer are related to upregulation of several downstream signaling cascades. Therefore, the knock-down efficacy by means of downregulation of the ERK phosphorylation was evaluated in the lung KRAS^{G12V} mutant cell line CMT167 (Fig. 6D). Hence, while KRAS protein expression was maintained constant, a significant reduction in pERK/total ERK was displayed by western blot analysis in contrast to the blank HANA and untreated group.

In brief, the results of these studies showed the inhibition of the KRAS-GTP bound state, suggesting the degree of involvement of the mAb in reducing the proliferation and colony formation presumably after reaching intracellular compartments at levels that allow for endogenous KRAS inhibition.

3.5. *The functional activity is a consequence of the antiKRAS^{G12V} mAb intracellular delivery and target engagement, driven by the mAb entrapment into the HANAs*

Given the main goal of this work, which aims to achieve the intracellular delivery of functional mAbs, it is imperative to assess the capacity of the HANAs technology to release antiKRAS^{G12V} mAb at the intracellular level and interact with its epitope. Consequently, the intracellular levels of antiKRAS^{G12V} mAb upon tLyP1-HANAs and PEGtLyP1-HANAs treatment were quantified after 4 h of incubation at 37 °C (Fig. 7A). Notably, PEGtLyP1-HANAs exhibited the greatest efficacy (1.5 times higher than tLyP1-HANAs) in reaching intracellular domains. It is our hypothesis that the presentation of tLyP1 to the tumor microenvironment through the PEG spacer [58] is more appropriate than the one achieved for tLyp1-HAC16 in terms of its recognition by the NRP-1 receptors. This aligns with the PEGtLyP1-HANAs superior efficacy observed in the aforementioned functional studies. The lack of signal found for the free mAb further support the key role played by the HANAs in facilitating the access of mAbs into intracellular compartments. Finally, minimal signal was noted at 4 °C for blank and anti-KRASG12V mAb -loaded HANAs, indicating energy-dependent uptake [59] pathways as the primary mechanisms for internalization.

Following the confirmation of the intracellular delivery of anti-KRAS^{G12V} mAb, we found crucial to study its interaction with the KRAS^{G12V} oncoprotein. To do so, the CMT167 cell line was treated with the antiKRAS^{G12V} mAb PEGtLyP1-HANAs for up to 72 h. Fig. 7B illustrates time-dependent dynamics of target engagement, peaking at 48 h and diminishing thereafter. This reduction in engagement intensity suggests gradual mAb damage [60] followed by a decline in affinity for its target. Furthermore, the kinetics of release at the intracellular level

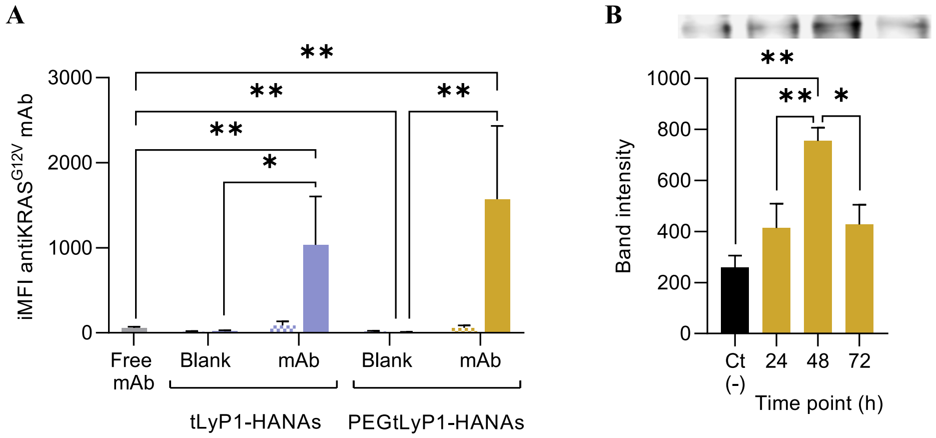

Fig. 7. Intracellular delivery of the antiKRAS^{G12V} mAb, followed by the engagement of the KRAS^{G12V} oncoprotein in the KRAS^{G12V}-mutant CMT167 cell line. **A.** Intracellular detection of antiKRAS^{G12V} mAb tLyP1-NAs and antiKRAS^{G12V} mAb PEGtLyP1-NAs after 4 h of exposure at 37 °C (filled bars) and 4 °C (squared bars). Cells were treated with 1 μM of antiKRAS^{G12V} mAb which corresponds to 0.075 mg/mL of tLyP1-HANAs. As controls, free antiKRAS^{G12V} mAb and blank tLyP1-NAs were used. Statistical differences were determined by using a Mann-Whitney *t*-test between antiKRAS^{G12V} mAb-HANAs *vs* free antiKRAS^{G12V} mAb or blank HANAs at 37 °C. iMFI integrated mean fluorescence intensity. **B.** Results of the target engagement study consisting on the analysis by immunoprecipitation (IP) of the interaction of KRAS^{G12V} protein with the antiKRAS^{G12V} mAb delivered from the PEGtLyP1-NAs. Raw images and band intensities of the western blot membrane of the amount of IP product determined after 24, 48, and 72 h. The negative control [Ct (−)] was done by immunoprecipitating 1 mg of the CMT167 cell lysate with the anti-mAb beads. Statistical differences were determined by using a one-way ANOVA between groups. Data are expressed as mean ± SEM (n ≥ 3).

induced by the disruptive intracellular conditions cannot be ruled out.

This assay plays a pivotal role in elucidating the mechanism of action of these novel candidates for KRAS targeting and inhibition. While prior delivery systems addressing other targets (BCR/ABL [20] or cMYC [19]), have provided valuable information into the fundamental mechanism, our study validates this mechanism specifically for KRAS.

Overall, the greatest capacity of PEGtLyP1-NAs to inhibit cell proliferation, colony formation and knockdown pERK was aligned with an efficient intracellular delivery of the antiKRAS^{G12V} mAb. Moreover, the capacity of the delivered mAb molecules to recognize the intracellular target represents a clear assessment of the potential of the HANA's nanotechnology. In consequence, the most promising candidate (PEGtLyP1-NAs) was selected to validate its *in vivo* efficacy in a relevant KRAS^{G12V} mutant model.

3.6. antiKRAS^{G12V} mAb -loaded HANAs reduce the tumor growth on a subcutaneous pancreatic cancer model

Previous investigations into KRAS inhibition have demonstrated reduced phosphorylation of downstream proteins in the RAS/RAF/MEK pathway. However, a paradoxical outcome has been observed, wherein KRAS blocking fosters compensatory mechanisms, leading to drug resistance through either innate or acquired means. [53,61] Consequently, our hypothesis posits that the use of antiKRAS^{G12V} mAb-PEGtLyP1-NAs for targeting the KRAS^{G12V} mutation would allow the blockage of KRAS and mitigate compensatory mechanisms.

The antitumor efficacy of the aforementioned therapeutics was assessed in a subcutaneous CFPAC-1 pancreatic tumor model harboring the KRAS^{G12V} mutant (**Fig. 8**) [62,63]. As the enhanced tumor accumulation of these NPs relies on the tLyP1 recognition by the NRP-1 receptor, NRP-1 expression in CFPAC-1 cells was previously confirmed in cell culture by flow cytometry and in subcutaneously implanted tumors by immunoblot (Suppl. Fig. 5), aligning with previous reports [64]. Since mAbs cannot cross cell membranes and, hence, no therapeutic activity is expected [21], free mAb was not administered. The results indicate that the intravenous administration of antiKRAS^{G12V} mAb-PEGtLyP1-NAs as a monotherapy effectively impeded tumor progression, resulting in a significantly reduced tumor volume (40%) at the endpoint. This inhibitory effect can be attributed to the successful *in vivo* blockade of the KRAS^{G12V} protein within the tumor tissue. None of the treated animals showed signs of toxicity nor body weight change over the experiment (Suppl. Fig. 6). In summary, our results underscore the potent antitumor activity of antiKRAS^{G12V} mAb-PEGtLyP1-HANAs in a KRAS^{G12V}-mutant pancreatic-bearing mice model.

In the realm of KRAS-targeted therapies, tackling the KRAS^{G12V} mutation remains a therapeutic enigma. Our pioneering technology addresses the G12V-mutation specifically, utilizing an antiKRAS^{G12V} mAb. This novel approach not only block KRAS^{G12V} while exhibiting a favorable safety profile. In the context of recent findings suggesting a suboptimal.

patient response to KRAS^{G12C} inhibitors, [10] our mAb-based nanotechnology approach brings new hopes towards a therapeutic option addressing other mutations.

4. Conclusions

We disclose a new versatile nanotechnology specifically designed for the intracellular delivery of mAbs. The HANAs technology enables a remarkable loading of mAbs (bevacizumab and antiKRAS^{G12V} mAb) while incorporating a tumor penetrating peptide (t-LyP1) on the NP surface. The antiKRAS^{G12V} mAb loaded HANAs were able to reduce proliferation and colony formation across a panel of KRAS^{G12V} mutant cell lines. Intracellular staining and target engagement assays shed light to the underlying mechanism of the antiKRAS^{G12V} mAb, confirming its specific binding to the KRAS^{G12V} oncoprotein. This *in vitro* behavior was translated into a significant tumor reduction *in vivo*. These findings validate the potential of KRAS^{G12V} blockade through our technology and propose them as a novel targeted cancer therapy. Our research offers a paradigm shift in the pursuit of effective KRAS-targeted interventions, representing a significant step towards personalized and impactful cancer therapeutics.

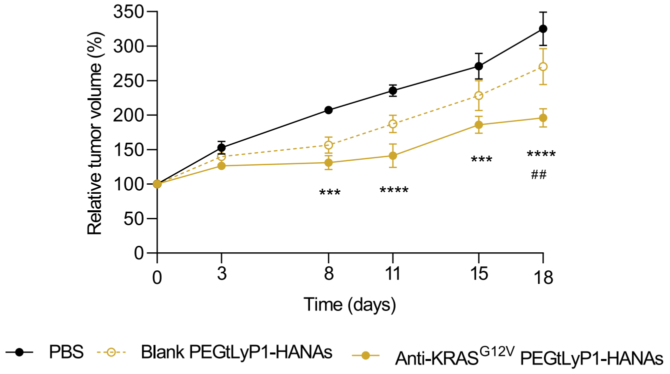

Fig. 8. *In vivo* efficacy studies in the KRAS^{G12V}-mutant subcutaneous pancreatic cancer model. Relative tumor volume over 18 days. Pancreatic tumor-bearing mice were intravenously injected with αKRAS^{G12V}-HANAs at αKRAS^{G12V} dose of 10 mg/kg, and the respective amount of blank-HANAs. As control, PBS was administered. Data represents mean ± SEM of 6–7 replicates. Statistical differences were determined by following a 2-way ANOVA following by a Tukey test. Significant differences between αKRAS^{G12V}-HANAs and PBS were considered for $***p < 0.001$, and $****p < 0.0001$, and αKRAS^{G12V}-HANAs and blank HANAs were considered for $## < 0.01$.

CRediT authorship contribution statement

Ana M. López-Estévez: Writing – review & editing, Writing – original draft, Visualization, Validation, Methodology, Investigation, Formal analysis, Data curation, Conceptualization. **Lucía Sanjurjo:** Writing – review & editing, Validation, Methodology, Investigation, Formal analysis. **Ángela Turrero:** Writing – review & editing, Methodology, Investigation, Formal analysis. **Iker Arriaga:** Writing – review & editing, Visualization, Methodology, Investigation, Formal analysis. **Nicola G.A. Abrescia:** Writing – review & editing, Visualization, Supervision, Formal analysis. **Ana Poveda:** Writing – review & editing, Visualization, Supervision, Investigation, Formal analysis. **Jesús Jiménez-Barbero:** Writing – review & editing, Visualization, Supervision, Formal analysis. **Anxo Vidal:** Writing – review & editing, Supervision, Project administration, Methodology. **Dolores Torres:** Writing – review & editing, Supervision, Project administration, Methodology. **María José Alonso:** Writing – review & editing, Writing – original draft, Validation, Supervision, Project administration, Methodology, Funding acquisition, Conceptualization.

Declaration of competing interest

M. J. Alonso is founder and shareholder of LiberaBio. The rest of the authors declare no conflict of interest.

Data availability

Data will be made available on request.

Acknowledgements

This work was supported by the government of Xunta de Galicia (Competitive Reference Groups, Ref.ED431C 2021/17) and the Spanish Ministry of Science, Innovation and Universities (Ref.SAF2017-86634-R), and by the Instituto de Salud Carlos III (ISCIII) and co-funded by EURONANOMED3 project EURONANOMED 2020-145: 2ˆ2-

INTRATARGET (Award N. AC20/00028). Financial support from the Xunta de Galicia (Centro singular de Investigación de Galicia acreditación 2019-2022) and the European Union (European Regional Development Fund - ERDF), is gratefully acknowledged (Ref.ED431G 2019/02). This work is part of the project Proof of Concept (PDC2021-120929-I00), funded by MICIU/AEI/ 10.13039/501100011033 and by the "European Union NextGenerationEU/PRTR". NCI-H441 and NCI-H1568 were kindly provided by Silve Vicent (University of Navarra, Center for Applied Medical Research, Program in Solid Tumors, Pamplona, Spain), and CMT167 by Paola Allavena (Clinical and Research Hospital Humanitas, Istituto di Ricovero e Cura a Carattere Scientifico (IRCCS), Milan, Italy). Authors would like to acknowledge the use of Nanotechnology and Surface Analysis services of Centro de Apoio Científico e Tecnolóxico á Investigación (CACTI-Universidade de Vigo). Ana M. López- Estévez acknowledges a predoctoral FPU grant from the Spanish Ministry of Science, Innovation and Universities (grant number FPU18/00095). Figures have been created with BioRender.com.

Appendix A. Supplementary data

Supplementary data to this article can be found online at https://doi.org/10.1016/j.jconrel.2024.07.032.

References

[1] A.D. Cox, S.W. Fesik, A.C. Kimmelman, J. Luo, C.J. Der, Drugging the undruggable RAS : mission possible ? Nat. Rev. Drug Discov. (2014) https://doi.org/10.1038/nrd4389.

[2] S.R. Punekar, V. Velcheti, B.G. Neel, K.K. Wong, The current state of the art and future trends in RAS-targeted cancer therapies, Nat. Rev. Clin. Oncol. 19 (2022) 637–655, https://doi.org/10.1038/s41571-022-00671-9.

[3] K.M. Haigis, K.R. Kendall, Y. Wang, A. Cheung, M.C. Haigis, J.N. Glickman, M. Niwa-Kawakita, A. Sweet-Cordero, J. Sebolt-Leopold, K.M. Shannon, J. Settleman, M. Giovannini, T. Jacks, Differential effects of oncogenic K-Ras and N-Ras on proliferation, differentiation and tumor progression in the colon, Nat. Genet. 40 (2008) 600–608, https://doi.org/10.1038/ng.115.

[4] Y. Matsuo, P.M. Campbell, R.A. Brekken, B. Sung, M.M. Ouellette, J.B. Fleming, B. B. Aggarwal, C.J. Der, S. Guha, K-Ras promotes angiogenesis mediated by immortalized human pancreatic epithelial cells through mitogen-activated protein kinase signaling pathways, Mol. Cancer Res. 7 (2009) 799–808, https://doi.org/10.1158/1541-7786.MCR-08-0577.

[5] M. Drosten, A. Dhawahir, E.Y.M. Sum, J. Urosevic, C.G. Lechuga, L.M. Esteban, E. Castellano, C. Guerra, E. Santos, M. Barbacid, Genetic analysis of Ras signalling pathways in cell proliferation, migration and survival, EMBO J. 29 (2010) 1091–1104, https://doi.org/10.1038/emboj.2010.7.

[6] S. Pant, Z.A. Wainberg, C.D. Weekes, M. Furqan, P.M. Kasi, C.E. Devoe, A.D. Leal, V. Chung, O. Basturk, H. Van Wyk, A.M. Tavares, L.M. Seenappa, J.R. Perry, T. Kheoh, L.K. McNeil, E. Welkowsky, P.C. DeMuth, C.M. Haqq, E.M. O'Reilly, Lymph-node-targeted, mKRAS-specific amphiphile vaccine in pancreatic and colorectal cancer: the phase 1 AMPLIFY-201 trial, Nat. Med. 30 (2024) 531–542, https://doi.org/10.1038/s41591-023-02760-3.

[7] M. Salmón, R. Álvarez-Díaz, C. Fustero-Torre, O. Brehey, C.G. Lechuga, M. Sanclemente, F. Fernández-García, A. López-García, M.C. Martín-Guijarro, S. Rodríguez-Perales, E. Bousquet-Mur, L. Morales-Cacho, F. Mulero, F. Al-Shahrour, L. Martínez, O. Domínguez, E. Caleiras, S. Ortega, C. Guerra, M. Musteanu, M. Drosten, M. Barbacid, Kras oncogene ablation prevents resistance in advanced lung adenocarcinoma, J. Clin. Invest (2023), https://doi.org/10.1172/JCI164413.

[8] FDA, LUMAKRAS™ (Sotorasib) - FDA Label, 2021, https://doi.org/10.1358/dof.2021.46.7.3301489.

[9] FDA, KRAZATI™ (Adagrasib) - FDA Label, 2022.

[10] J.H. Strickler, H. Satake, T.J. George, R. Yaeger, A. Hollebecque, I. Garrido-Laguna, M. Schuler, T.F. Burns, A.L. Coveler, G.S. Falchook, M. Vincent, Y. Sunakawa, L. Dahan, D. Bajor, S.-Y. Rha, C. Lemech, D. Juric, M. Rehn, G. Ngarmchamnanrith, P. Jafarinasabian, Q. Tran, D.S. Hong, Sotorasib in KRAS p.G12C–mutated advanced pancreatic cancer, N. Engl. J. Med. 388 (2023) 33–43, https://doi.org/10.1056/nejmoa2208470.

[11] R.M. Haley, A. Chan, M.M. Billingsley, N. Gong, M.S. Padilla, E.H. Kim, H. Wang, D. Yin, K.J. Wangensteen, A. Tsourkas, M.J. Mitchell, Lipid nanoparticle delivery of small proteins for potent in vivo RAS inhibition, ACS Appl. Mater. Interfaces (2023), https://doi.org/10.1021/acsami.3c01501.

[12] S. Anthiya, S.C. Öztürk, H. Yanik, E. Tavukcuoglu, A. Şahin, D. Datta, K. Charisse, D.M. Álvarez, M.I. Loza, A. Calvo, E. Sulheim, S. Loevenich, G. Klinkenberg, R. Schmid, M. Manoharan, G. Esendağlı, M.J. Alonso, Targeted siRNA lipid nanoparticles for the treatment of KRAS-mutant tumors, J. Control. Release 357 (2023) 67–83, https://doi.org/10.1016/j.jconrel.2023.03.016.

[13] A.S. Silva, K.E. Shopsowitz, S. Correa, S.W. Morton, E.C. Dreaden, T. Casimiro, A. Aguiar-Ricardo, P.T. Hammond, Rational design of multistage drug delivery vehicles for pulmonary RNA interference therapy, Int. J. Pharm. 591 (2020) 119989, https://doi.org/10.1016/j.ijpharm.2020.119989.

[14] Y. Sasayama, M. Hasegawa, E. Taguchi, K. Kubota, T. Kuboyama, T. Naoi, H. Yabuuchi, N. Shimai, M. Asano, A. Tokunaga, T. Ishii, J. Enokizono, In vivo activation of PEGylated long circulating lipid nanoparticle to achieve efficient siRNA delivery and target gene knock down in solid tumors, J. Control. Release 311–312 (2019) 245–256, https://doi.org/10.1016/j.jconrel.2019.09.004.

[15] M.E. Gilles, L. Hao, K. Brown, J. Lim, S.N. Bhatia, F.J. Slack, Tumor penetrating nanomedicine targeting both an oncomi R and an oncogene in pancreatic cancer, Oncotarget 10 (2019) 5349–5358, https://doi.org/10.18632/oncotarget.27160.

[16] J.H. Lo, L. Hao, M.D. Muzumdar, S. Raghavan, E.J. Kwon, E.M. Pulver, F. Hsu, A. J. Aguirre, B.M. Wolpin, C.S. Fuchs, W.C. Hahn, T. Jacks, S.N. Bhatia, IRGD-guided tumor-penetrating nanocomplexes for therapeutic siRNA delivery to pancreatic cancer, Mol. Cancer Ther. 17 (2018) 2377–2388, https://doi.org/10.1158/1535-7163.MCT-17-1090.

[17] S.M. Shin, D.K. Choi, K. Jung, J. Bae, J.S. Kim, S.W. Park, K.H. Song, Y.S. Kim, Antibody targeting intracellular oncogenic Ras mutants exerts anti-tumour effects after systemic administration, Nat. Commun. 8 (2017) 1–14, https://doi.org/10.1038/ncomms15090.

[18] Y.W. Kang, J.E. Lee, K.H. Jung, M.K. Son, S.M. Shin, S.J. Kim, Z. Fang, H.H. Yan, J. H. Park, B. Han, M.J. Cheon, M.G. Woo, J.H. Lim, Y.S. Kim, S.S. Hong, KRAS targeting antibody synergizes anti-cancer activity of gemcitabine against pancreatic cancer, Cancer Lett. 438 (2018) 174–186, https://doi.org/10.1016/j.canlet.2018.09.013.

[19] P. Chen, W. Yang, T. Hong, T. Miyazaki, A. Dirisala, K. Kataoka, H. Cabral, Nanocarriers escaping from hyperacidified endo/lysosomes in cancer cells allow tumor-targeted intracellular delivery of antibodies to therapeutically inhibit c-MYC, Biomaterials 288 (2022) 121748, https://doi.org/10.1016/j.biomaterials.2022.121748.

[20] G. Jiang, Z. Huang, Y. Yuan, K. Tao, W. Feng, Intracellular delivery of anti-BCR/ABL antibody by PLGA nanoparticles suppresses the oncogenesis of chronic myeloid leukemia cells, J. Hematol. Oncol. 14 (2021) 1–18, https://doi.org/10.1186/s13045-021-01150-x.

[21] Á. Molina-Crespo, A. Cadete, D. Sarrio, M. Gámez-Chiachio, L. Martinez, K. Chao, A. Olivera, A. Gonella, E. Díaz, J. Palacios, P.K. Dhal, M. Besev, M. Rodríguez-Serrano, M.L. García Bermejo, J.C. Triviño, A. Cano, M. García-Fuentes, O. Herzberg, D. Torres, M.J. Alonso, G. Moreno-Bueno, Intracellular delivery of an antibody targeting Gasdermin-B reduces HER2 breast cancer aggressiveness, Clin. Cancer Res. 25 (2019) 4846–4858, https://doi.org/10.1158/1078-0432.CCR-18-2381.

[22] D. Rafael, S. Montero, P. Carcavilla, F. Andrade, J. German-Cortés, Z.V. Diaz-Riascos, J. Seras-Franzoso, M. Llaguno, B. Fernández, A. Pereira, E.F. Duran-Lara, S. Schwartz, I. Abasolo, Intracellular delivery of anti-Kirsten rat sarcoma antibodies mediated by polymeric micelles exerts strong in vitro and in vivo anti-tumorigenic activity in Kirsten rat sarcoma-mutated cancers, ACS Appl. Mater. Interfaces 15 (2023) 10398–10413, https://doi.org/10.1021/acsami.2c19897.

[23] B.J. Raphael, R.H. Hruban, A.J. Aguirre, R.A. Moffitt, J.J. Yeh, C. Stewart, A.G. Robertson, A.D. Cherniack, M. Gupta, G. Getz, S.B. Gabriel, M. Meyerson, C. Cibulskis, S.S. Fei, T. Hinoue, H. Shen, P.W. Laird, S. Ling, Y. Lu, G.B. Mills, R. Akbani, P. Loher, E.R. Londin, I. Rigoutsos, A.G. Telonis, E.A. Gibb, A. Goldenberg, A.M. Mezlini, K.A. Hoadley, E. Collisson, E. Lander, B.A. Murray, J. Hess, M. Rosenberg, L. Bergelson, H. Zhang, J. Cho, G. Tiao, J. Kim, D. Livitz, I. Leshchiner, B. Reardon, E. Van Allen, A. Kamburov, R. Beroukhim, G. Saksena, S.E. Schumacher, M.S. Noble, D.I. Heiman, N. Gehlenborg, J. Kim, M.S. Lawrence, V. Adsay, G. Petersen, D. Klimstra, N. Bardeesy, M.D.M. Leiserson, R. Bowlby, K. Kasaian, I. Birol, K.L. Mungall, S. Sadeghi, J.N. Weinstein, P.T. Spellman, Y. Liu, L. T. Amundadottir, J. Tepper, A.D. Singhi, R. Dhir, D. Paul, T. Smyrk, L. Zhang, P. Kim, J. Bowen, J. Frick, J.M. Gastier-Foster, M. Gerken, K. Lau, K.M. Leraas, T.M. Lichtenberg, N.C. Ramirez, J. Renkel, M. Sherman, L. Wise, P. Yena, E. Zmuda, J. Shih, A. Ally, M. Balasundaram, R. Carlsen, A. Chu, E. Chuah, A. Clarke, N. Dhalla, R.A. Holt, S.J.M. Jones, D. Lee, Y. Ma, M.A. Marra, M. Mayo, R.A. Moore, A.J. Mungall, J.E. Schein, P. Sipahimalani, A. Tam, N. Thiessen, K. Tse, T. Wong, D. Brooks, J.T. Auman, S. Balu, T. Bodenheimer, D.N. Hayes, A.P. Hoyle, S.R. Jefferys, C.D. Jones, S. Meng, P.A. Mieczkowski, L.E. Mose, C.M. Perou, A.H. Perou, J. Roach, Y. Shi, J. V. Simons, T. Skelly, M.G. Soloway, D. Tan, U. Veluvolu, J.S. Parker, M.D. Wilkerson, A. Korkut, Y. Senbabaoglu, P. Burch, R. McWilliams, K. Chaffee, A. Oberg, W. Zhang, M.C. Gingras, D.A. Wheeler, L. Xi, M. Albert, J. Bartlett, H. Sekhon, Y. Stephen, Z. Howard, M. Judy, A. Breggia, R.T. Shroff, S. Chudamani, J. Liu, L. Lolla, R. Naresh, T. Pihl, Q. Sun, Y. Wan, Y. Wu, S. Jennifer, K. Roggin, K.F. Becker, M. Behera, J. Bennett, L. Boice, E. Burks, C.G. Carlotti Junior, J. Chabot, D. Pretti da Cunha Tirapelli, J. Sebastião dos Santos, M. Dubina, J. Eschbacher, M. Huang, L. Huelsenbeck-Dill, R. Jenkins, A. Karpov, R. Kemp, V. Lyadov, S. Maithel, G. Manikhas, E. Montgomery, H. Noushmehr, A. Osunkoya, T. Owonikoko, O. Paklina, O. Potapova, S. Ramalingam, W.K. Rathmell, K. Rieger-Christ, C. Saller, G. Setdikova, A. Shabunin, G. Sica, T. Su, T. Sullivan, P. Swanson, K. Tarvin, M. Tavobilov, L.B. Thorne, S. Urbanski, O. Voronina, T. Wang, D. Crain, E. Curley, J. Gardner, D. Mallery, S. Morris, J. Paulauskis, R. Penny, C. Shelton, T. Shelton, K.P. Janssen, O. Bathe, N. Bahary, J. Slotta-Huspenina, A. Johns, H. Hibshoosh, R.F. Hwang, A. Sepulveda, A. Radenbaugh, S.B. Baylin, M. Berrios, M.S. Bootwalla, A. Holbrook, P.H. Lai, D.T. Maglinte, S. Mahurkar, T.J. Triche, D.J. Van Den Berg, D.J. Weisenberger, L. Chin, R. Kucherlapati, M. Kucherlapati, A. Pantazi, P. Park, G. Saksena, D. Voet, P. Lin, S. Frazer, T. Defreitas, S. Meier, L. Chin, S.Y. Kwon, Y.H. Kim, S.J. Park, S.S. Han, S.H. Kim, H. Kim, E. Furth, M. Tempero, C. Sander, A. Biankin, D. Chang, P. Bailey, A. Gill, J. Kench, S. Grimmond, A. Johns, A.P. Cancer Genome Initiative (APGI), R. Postier, R. Zuna, H. Sicotte, J.A. Demchok, M.L. Ferguson, C.M. Hutter, K.R. Mills Shaw, M. Sheth, H.J. Sofia, R.

Tarnuzzer, Z. Wang, L. Yang, J. Zhang, I. Felau, J.C. Zenklusen, Integrated genomic characterization of pancreatic ductal adenocarcinoma, Cancer Cell 32 (2017) 185–203.e13. doi:https://doi.org/10.1016/j.ccell.2017.07.007.

[24] Z. Zhang, H. Zhang, X. Liao, H.I.I. Tsai, KRAS mutation: the booster of pancreatic ductal adenocarcinoma transformation and progression, Front. Cell Dev. Biol. 11 (2023), https://doi.org/10.3389/fcell.2023.1147676.

[25] A.M. López-Estévez, Y. Zhang, M. Medel, I. Arriaga, L. Sanjurjo, N.G.A. Abrescia, M.J. Vicent, D. Ouyang, D. Torres, M.J. Alonso, Engineered hyaluronic acid-based nanoassemblies for monoclonal antibody delivery - design, characterization, and biological insights, Nano Res. (2024), https://doi.org/10.1007/s12274-024-6826-8.

[26] C. Teijeiro-valiño, R. Novoa-carballal, E. Borrajo, A. Vidal, M. Alonso-nocelo, M. De, F. Freire, P.P. Lopez-casas, M. Hidalgo, N. Csaba, M. José, A multifunctional drug nanocarrier for efficient anticancer therapy, J. Control. Release (2018), https://doi.org/10.1016/j.jconrel.2018.12.002.

[27] P. He, Q. Lei, B. Yang, T. Shang, J. Shi, Q. Ouyang, W. Wang, L. Xue, F. Kong, Z. Li, J. Huang, L. Liu, J. Guo, C.J. Brinker, K. Liu, W. Zhu, Dual-stage irradiation of size-switchable albumin nanocluster for cascaded tumor enhanced penetration and Photothermal therapy, ACS Nano (2022), https://doi.org/10.1021/acsnano.2c02965.

[28] C. Jiang, X. Wang, B. Teng, Z. Wang, F. Li, Y. Zhao, Y. Guo, Q. Zeng, Peptide-targeted high-density lipoprotein nanoparticles for combinatorial treatment against metastatic breast cancer, ACS Appl. Mater. Interfaces 1 (2021) acsami.1c02074, https://doi.org/10.1021/acsami.1c02074.

[29] M.D. Abràmoff, P.J. Magalhães, S.J. Ram, Image processing with imageJ, Biophotonics Int. 11 (2004) 36–41, https://doi.org/10.1201/9781420005615.ax4.

[30] M. Durán-Lobato, A.M. López-Estévez, A.S. Cordeiro, T.G. Dacoba, J. Crecente-Campo, D. Torres, M.J. Alonso, Nanotechnologies for the delivery of biologicals: historical perspective and current landscape, Adv. Drug Deliv. Rev. 176 (2021) 113899, https://doi.org/10.1016/j.addr.2021.113899.

[31] A.M. López-Estévez, P. Lapuhs, L. Pineiro-Alonso, M.J. Alonso, Personalized cancer nanomedicine: overcoming biological barriers for intracellular delivery of biopharmaceuticals, Adv. Mater. (2023), https://doi.org/10.1002/adma.202309355.

[32] M.J. Alonso, Intracellular delivery of biological, in: Drugs Carriers Med. Biol. Gordon Conf, 2022.

[33] M.J. Alonso, Reaching undruggable targets in personalized oncology using nanotechnology, in: Nanomed Eur., Liverpool, 2023.

[34] M.J. Alonso, Advanced therapies and personalized medicine: the role of pharmaceutical nanotechnology, in: ADRIATELF Symnposium, Trieste, 2023.

[35] J. Zhang, L. Wang, H. Fai Chan, W. Xie, S. Chen, C. He, Y. Wang, M. Chen, Co-delivery of paclitaxel and tetrandrine via iRGD peptide conjugated lipid-polymer hybrid nanoparticles overcome multidrug resistance in cancer cells, Sci. Rep. 7 (2017) 1–14, https://doi.org/10.1038/srep46057.

[36] S.D. Perrault, C. Walkey, T. Jennings, H.C. Fischer, W.C.W. Chan, Mediating tumor targeting efficiency of nanoparticles through design, Nano Lett. 9 (2009) 1909–1915, https://doi.org/10.1021/nl900031y.

[37] A. Schädlich, H. Caysa, T. Mueller, F. Tenambergen, C. Rose, A. Göpferich, J. Kuntsche, K. Mäder, Tumor accumulation of NIR fluorescent PEG-PLA nanoparticles: impact of particle size and human xenograft tumor model, ACS Nano 5 (2011) 8710–8720, https://doi.org/10.1021/nn2026353.

[38] E.A. Sykes, J. Chen, G. Zheng, W.C.W. Chan, Investigating the impact of nanoparticle size on active and passive tumor targeting efficiency, ACS Nano 8 (2014) 5696–5706, https://doi.org/10.1021/nn500299p.

[39] J. Pang, H. Xing, Y. Sun, S. Feng, S. Wang, Non-small cell lung cancer combination therapy: hyaluronic acid modified, epidermal growth factor receptor targeted, pH sensitive lipid-polymer hybrid nanoparticles for the delivery of erlotinib plus bevacizumab, Biomed. Pharmacother. 125 (2020) 109861, https://doi.org/10.1016/j.biopha.2020.109861.

[40] A. Baião, F. Sousa, A.V. Oliveira, C. Oliveira, B. Sarmento, Effective intracellular delivery of bevacizumab via PEGylated polymeric nanoparticles targeting the CD44v6 receptor in colon cancer cells, Biomater. Sci. 8 (2020) 3720–3729, https://doi.org/10.1039/D0BM00556H.

[41] O. Tirosh, Y. Barenholz, J. Katzhendler, A. Priev, Hydration of polyethylene glycol-grafted liposomes, Biophys. J. 74 (1998) 1371–1379, https://doi.org/10.1016/S0006-3495(98)77849-X.

[42] H. Harada, M. Takahashi, CD44-dependent intracellular and extracellular catabolism of hyaluronic acid by hyaluronidase-1 and -2, J. Biol. Chem. 282 (2007) 5597–5607, https://doi.org/10.1074/jbc.M608358200.

[43] J.P. Laye, J.H. Gill, Phospholipase A2 expression in tumours: a target for therapeutic intervention? Drug Discov. Today 8 (2003) 710–716, https://doi.org/10.1016/S1359-6446(03)02754-5.

[44] M. Mumtaz Virk, E. Reimhult, Phospholipase A2-induced degradation and release from lipid-containing polymersomes, Langmuir 34 (2018) 395–405, https://doi.org/10.1021/acs.langmuir.7b03893.

[45] A.R. Nicholas, M.J. Scott, N.I. Kennedy, M.N. Jones, Effect of grafted polyethylene glycol (PEG) on the size, encapsulation efficiency and permeability of vesicles, Biochim. Biophys. Acta Biomembr. 1463 (2000) 167–178, https://doi.org/10.1016/S0005-2736(99)00192-3.

[46] L. Liu, C. Zhou, X. Xia, Y. Liu, Self-assembled lecithin/chitosan nanoparticles for oral insulin delivery: preparation and functional evaluation, Int. J. Nanomedicine 11 (2016) 761–769, https://doi.org/10.2147/IJN.S96146.

[47] Y. Gerelli, M.T. Di Bari, A. Deriu, L. Cantu, P. Colombo, C. Como, S. Motta, F. Sonvico, R. May, Structure and organization of phospholipid/polysaccharide nanoparticles, J. Phys. Condens. Matter 20 (2008), https://doi.org/10.1088/0953-8984/20/10/104211.

[48] S. Mitragotri, P.A. Burke, R. Langer, Overcoming the challenges in administering biopharmaceuticals: formulation and delivery strategies, Nat. Rev. Drug Discov. 13 (2014) 655–672, https://doi.org/10.1038/nrd4363.

[49] F. Sousa, P. Castro, P. Fonte, P.J. Kennedy, M.T. Neves-Petersen, B. Sarmento, Nanoparticles for the delivery of therapeutic antibodies: dogma or promising strategy? Expert Opin. Drug Deliv. 14 (2017) 1163–1176, https://doi.org/10.1080/17425247.2017.1273345.

[50] J. Hallin, L.D. Engstrom, L. Hargi, A. Calinisan, R. Aranda, D.M. Briere, N. Sudhakar, V. Bowcut, B.R. Baer, J.A. Ballard, M.R. Burkard, J.B. Fell, J. P. Fischer, G.P. Vigers, Y. Xue, S. Gatto, J. Fernandez-Banet, A. Pavlicek, K. Velastagui, R.C. Chao, J. Barton, M. Pierobon, E. Baldelli, E.F. Patricoin, D. P. Cassidy, M.A. Marx, I.I. Rybkin, M.L. Johnson, S.H. Ignatius, P. Lito, K. P. Papadopoulos, P.A. Jänne, P. Olson, J.G. Christensen, The KRASG12C inhibitor MRTX849 provides insight toward therapeutic susceptibility of KRAS-mutant cancers in mouse models and patients, Cancer Discov. 10 (2020) 54–71, https://doi.org/10.1158/2159-8290.CD-19-1167.

[51] H.S. Solanki, E.A. Welsh, B. Fang, V. Izumi, L. Darville, B. Stone, R. Franzese, S. Chavan, F. Kinose, D. Imbody, J.M. Koomen, U. Rix, E.B. Haura, Cell type-specific adaptive signaling responses to KRASG12C inhibition, Clin. Cancer Res. 27 (2021) 2533–2548, https://doi.org/10.1158/1078-0432.CCR-20-3872.

[52] Y. Zhao, Y.R. Murciano-Goroff, J.Y. Xue, A. Ang, J. Lucas, T.T. Mai, A.F. Da Cruz Paula, A.Y. Saiki, D. Mohn, P. Achanta, A.E. Sisk, K.S. Arora, R.S. Roy, D. Kim, C. Li, L.P. Lim, M. Li, A. Bahr, B.R. Loomis, E. de Stanchina, J.S. Reis-Filho, B. Weigelt, M. Berger, G. Riely, K.C. Arbour, J.R. Lipford, B.T. Li, P. Lito, Diverse alterations associated with resistance to KRAS(G12C) inhibition, Nature 599 (2021) 679–683, https://doi.org/10.1038/s41586-021-04065-2.

[53] N. Tanaka, J.J. Lin, C. Li, M.B. Ryan, J. Zhang, L.A. Kiedrowski, A.G. Michel, M. U. Syed, K.A. Fella, M. Sakhi, I. Baiev, D. Juric, J.F. Gainor, S.J. Klempner, J. K. Lennerz, G. Siravegna, L. Bar-Peled, A.N. Hata, R.S. Heist, R.B. Corcoran, Clinical acquired resistance to krasg12c inhibition through a novel kras switch-ii pocket mutation and polyclonal alterations converging on ras–mapk reactivation, Cancer Discov. 11 (2021) 1913–1922, https://doi.org/10.1158/2159-8290.CD-21-0365.

[54] J.B. Blaquier, A.F. Cardona, G. Recondo, Resistance to KRASG12C inhibitors in non-small cell lung cancer, Front. Oncol. 11 (2021) 1–9, https://doi.org/10.3389/fonc.2021.787585.

[55] A. Singh, P. Greninger, D. Rhodes, L. Koopman, S. Violette, N. Bardeesy, J. Settleman, A gene expression signature associated with "K-Ras addiction" reveals regulators of EMT and tumor cell survival, Cancer Cell 15 (2009) 489–500, https://doi.org/10.1016/j.ccr.2009.03.022.

[56] L. Zeng, J. Li, J. Li, Q. Zhang, C. Qian, W. Wu, Z. Lin, J. Liang, Y. Chen, K. Huang, Effective suppression of the kirsten rat sarcoma viral oncogene in pancreatic tumor cells via targeted small interfering rna delivery using nanoparticles, Pancreas 44 (2015) 250–259, https://doi.org/10.1097/MPA.0000000000000241.

[57] L. Zeng, J. Li, Y. Wang, C. Qian, Y. Chen, Q. Zhang, W. Wu, Z. Lin, J. Liang, X. Shuai, K. Huang, Combination of siRNA-directed Kras oncogene silencing and arsenic-induced apoptosis using a nanomedicine strategy for the effective treatment of pancreatic cancer, nanomedicine nanotechnology, Biol. Med. 10 (2014) 463–472, https://doi.org/10.1016/j.nano.2013.08.007.

[58] C. Barth, H. Spreen, D. Mulac, L. Keuter, M. Behrens, H.U. Humpf, K. Langer, Spacer length and serum protein adsorption affect active targeting of trastuzumab-modified nanoparticles, Biomater. Biosyst. 5 (2022) 100032, https://doi.org/10.1016/j.bbiosy.2021.100032.

[59] S. Snipstad, S. Hak, H. Baghirov, E. Sulheim, Ý. Mørch, S. Lélu, E. von Haartman, M. Bäck, K.P.R. Nilsson, A.S. Klymchenko, C. de Lange Davies, A.K.O. Åslund, Labeling nanoparticles: dye leakage and altered cellular uptake, Cytom. Part A. 91 (2017) 760–766, https://doi.org/10.1002/cyto.a.22853.

[60] Z. Zhang, X. Zhang, X. Fang, M. Niimi, Y. Huang, H. Piao, S. Gao, J. Fan, J. Yao, Glutathione inhibits antibody and complement-mediated immunologic cell injury via multiple mechanisms, Redox Biol. 12 (2017) 571–581, https://doi.org/10.1016/j.redox.2017.03.030.

[61] M.M. Awad, S. Liu, I.I. Rybkin, K.C. Arbour, J. Dilly, V.W. Zhu, M.L. Johnson, R. S. Heist, T. Patil, G.J. Riely, J.O. Jacobson, X. Yang, N.S. Persky, D.E. Root, K. E. Lowder, H. Feng, S.S. Zhang, K.M. Haigis, Y.P. Hung, L.M. Sholl, B.M. Wolpin, J. Wiese, J. Christiansen, J. Lee, A.B. Schrock, L.P. Lim, K. Garg, M. Li, L. D. Engstrom, L. Waters, J.D. Lawson, P. Olson, P. Lito, S.-H.I. Ou, J.G. Christensen, P.A. Jänne, A.J. Aguirre, Acquired resistance to KRAS G12C inhibition in cancer, N. Engl. J. Med. 384 (2021) 2382–2393, https://doi.org/10.1056/nejmoa2105281.

[62] R. Sinha, A. Luna, N. Schultz, C. Sander, A pan-cancer survey of cell line tumor similarity by feature-weighted molecular profiles, Cell Reports Methods 1 (2021) 100039, https://doi.org/10.1016/j.crmeth.2021.100039.

[63] Cellosaurus CFPAC-1 (CVCL_1119), (2024). https: //www.cellosaurus.org/CVCL_1119 (accessed December 18, 2023).

[64] L.H. He, Y.L. He, W.H. Zuo, Y. Kang, H. Xue, L.Y. Wang, Y.L. Zhang, Y. Meng, Neuropilin1 silencing impairs the proliferation and migration of cells in pancreatic cancer, J. Clin. Lab. Anal. 34 (2020), https://doi.org/10.1002/jcla.23394.